Characterization of Subdaily Rainfall Events over Central Africa: Duration, Intensity, Amount, and Spatial Scale of the Storm Types🖉

FRANÇOIS XAVIER MENGOUNA🅾,[a] N. PHILIPPON🅾,[b] DERBETINI A. VONDOU🅾,[a] VINCENT MORON🅾,[c]
MARLON MARANAN🅾,[d] AND ANDREAS H. FINK🅾[d]

[a] *Laboratory of Environmental Modeling and Atmospheric Physics, Department of Physics, University of Yaoundé I, Yaoundé, Cameroon*
[b] *Institut des Geosciences de l'Environnement, Universite Grenoble Alpes, CNRS, IRD, Grenoble INP, Grenoble, France*
[c] *Aix-Marseille University, CNRS, IRD, INRAE, Coll. de France, CEREGE, Aix en Provence, France*
[d] *Karlsruhe Institute of Technology, Karlsruhe, Germany*

ABSTRACT: Using half-hourly rainfall data from 14 automated weather stations over central Africa, rainfall events [≥ 0.1 mm (30 min)$^{-1}$] characteristics are explored. A total of 10 096 wet events (WEs) were identified and classified into six storm types (STs), mostly discretized by their duration and intensity. ST 1 is very short (<1.5 h) with low rainfall intensities over a small area and contributes the least to the total rainfall (7%) but is by far the most frequent (70% of the WEs). ST 2 is short (~ 1.5 h) and sudden with very intense rains and of medium spatial scale (<200 km). ST 3 is short and of medium scale too but with low intensities and rainfall amounts. ST 4 and ST 5 are of large scale and long (~ 3–4 h), with high rainfall amounts so that they contribute the most to the total rainfall (29% and 20%). Last, ST 6 is the largest, longest, and rainiest, although moderately intense. A complementary classification is performed on lagged gridded rainfall fields from IMERG to document the possible space–time evolution of the rainfall field during the life cycle of WEs. Four spatial types are identified. Spatial type 1 gathers the most frequent, less intense ones. Spatial type 2 is far less frequent but pictures westward-moving rainfall patterns, probably associated with mesoscale convective systems. Two spatial types (3 and 4) are related to high-intensity near-stationary rainfall events, respectively, located to the southwest and northwest of the stations. ST 4 is mostly present at stations close to the Atlantic Ocean.

KEYWORDS: Hydrometeorology; In situ atmospheric observations; Clustering; Thunderstorms; Mesoscale systems

1. Introduction

After the Amazon rain forest, central Africa (CA) harbors the second largest tropical rain forest in the Congo and some adjacent river basins, which has the potential to modulate regional- and global-scale climates through its role in the transfer of energy, moisture, and carbon (Malhi et al. 2013; Mayaux et al. 2013). Tropical deforestation has been linked to a reduction in rainfall across much of the tropics. The threat is most acute in the Congo basin, where rapid deforestation is predicted in the coming years and could reduce rainfall by up to 10% by the end of the century (Smith et al. 2023). Moreover, CA is one of the three most important convective poles on the planet (Washington et al. 2013) but receives, on average, considerably less rainfall (1800–2200 mm yr^{-1}) than Amazonia and Indonesia (>2500 mm yr^{-1}) (Jackson et al. 2009; Zhou et al. 2014; Zhou et al. 2020; Adler et al. 2017; Nicholson 2022). Yet, this amount of rainfall is barely sufficient for maintaining evergreen forests, for reasons that remain unexplained nowadays (Nicholson 2022). Rainfall in CA is both influenced by regional and local circulations, such as the seasonal latitudinal migration of the tropical rain belt band (Nicholson 2022), the Walker circulation (Cook and Vizy 2016), the midlevel tropospheric jets over northern and southern CA (Kuete et al. 2020), and low-level westerlies (Pokam et al. 2014; Taguela et al. 2022). CA is a region in Africa that has been neglected in climate studies, perhaps due to a lower vulnerability to climatic extremes, data scarcity, and political instability (Farnsworth et al. 2011). However, the livelihoods of millions of people in CA depend on forest products and services. Their agricultural systems depend largely on rainfed agriculture due to the fact that the majority of farmers are smallholders with few financial resources, making them vulnerable to climate variability and change (Sonwa et al. 2012; Tamoffo et al. 2019; Mba et al. 2018; Mengouna et al. 2022; Fotso-Nguemo et al. 2023).

Mesoscale convective systems (MCSs), with their associated rainfall, wind, and lightning, are among CA's most devastating high-impact weather phenomena (Baidu et al. 2022). According to the study by Taylor et al. (2018), there has been a significant recent increase in the frequency of intense MCS over the Congo basin since February 1999. MCSs are the dominant rain-bearing systems in central equatorial Africa during the main rainy seasons (Hartman 2021). They produce over 50% of the total annual rainfall across most of the tropical belt (Feng et al. 2021). MCSs supply the water needed to sustain forest ecosystems and agriculture but can also cause devastating floods (Pielke and Downton 2000; Hu et al. 2021). Floods are the deadliest and costliest natural disaster in CA

🖉 Supplemental information related to this paper is available at the Journals Online website: https://doi.org/10.1175/JHM-D-23-0067.s1.

Corresponding author: François Xavier Mengouna, francoisxavier23@yahoo.com

countries (Cullmann et al. 2020). For example, on 21 August 2020, the flood affected nearly 2210 buildings and 12 376 victims over an area of 82 ha (Iroume et al. 2022). Most heavy rains are caused by MCSs, which generally produce convective and stratiform rainfall over several hundreds of kilometers (Houze et al. 2004; Nesbitt et al. 2006; Laing et al. 2011). In addition, according to the Sixth Assessment Report of the Intergovernmental Panel Climate Change (Trisos et al. 2022), heavy rainfall and flooding are projected to increase in CA as a response to climate change. This will further exacerbate the vulnerability of the population, who already has limited resources to cope with climatic disasters. Therefore, high-resolution rainfall measurements are fundamental to accurately assess and predict heavy rains in the future.

In contrast to other continuous atmospheric variables (e.g., temperature, humidity), rainfall has the key property of being discontinuous in space and time and thus has a high spatial and temporal variability (Trenberth and Zhang 2018; Tapiador et al. 2019). Any rainy event may be characterized by its total amount, duration, mean and maximum intensities, frequency of occurrence, and spatial footprint. Its duration is important information since it is closely related to the associated rain-bearing phenomenon and its horizontal scale and shift (Orlanski 1975; Trenberth and Zhang 2018). Therefore, evaluation from a subdaily event perspective could reveal information about rainfall organization and evolution that is lost in evaluations using fixed longer time scales (e.g., day, month) (Li et al. 2021). A rather large or stationary phenomenon leads to a relatively long duration. The mean and maximum intensities may be other distinct characteristics since the same amount of rain may fall over different durations, thus with a different mean intensity. For example, let us consider three theoretical rainfall events recorded at an hourly time scale, each giving a total of 60 mm of rainfall. The first one lasts less than 1 h (mean and maximum hourly intensity = 60 mm h^{-1}). The second one lasts 10 consecutive hours (mean hourly intensity of 6 mm h^{-1}), and the third one lasts 20 consecutive hours (mean hourly intensity of 3 mm h^{-1}). The latter event has by definition a maximum intensity of less than the first one. All these rainfall events may lead to different socioenvironmental impacts. We may expect, for example, that the risk of flash flood and societal and environmental vulnerabilities are far higher in the first case than in the second and third cases. The exact atmospheric processes and scales that lead to three hypothetical rainfall events might also be very different. Therefore, to characterize different types of rainy events, which can be strongly blurred at the daily time scale, it is important to analyze rainfall data at subhourly resolution. This is because an individual wet event usually lasts far less than a day across the tropical zone (Trenberth and Zhang 2018; Zhang and Wang 2021; Moron et al. 2021, 2023), as well as to understand the mechanisms underlying these rainfall events (Tapiador et al. 2019; Lengfeld et al. 2020; Li et al. 2021). Subhourly analysis may not only potentially help predict these different storm types from the meteorological point of view but also improve projections at decadal and longer time scales if their frequency/intensity is related to anthropogenic global warming (Taylor et al. 2018; Chen 2020; Zhang and Wang 2021).

Compared to the other tropical regions, knowledge about rainfall events over CA is still limited. Only a few studies have assessed rainfall characteristics over CA using either in situ data (e.g., Dezfuli 2011; Nicholson et al. 2018; Camberlin et al. 2019) or satellite rainfall estimates (McCollum et al. 2000; Nicholson et al. 2019; Igri et al. 2022; Yepdo Djomou et al. 2008), but most of the studies used data at daily or monthly time scales. To the best of our knowledge, no previous study has characterized rainfall at subdaily time scale in CA. One of the main reasons is due to the sparseness of in situ automatic weather stations recording rainfall at high temporal resolution (Bigot et al. 2016; Camberlin et al. 2019). But erroneous data, large gaps related either to measurement equipment malfunctioning (as blocking of the gauge by various debris or leaves) or their abandonment due to insufficient funding, often arising from fragile economies, or political conflicts in the region, strongly limit the availability of subdaily data (Washington et al. 2006; Malhi et al. 2013).

The main objective of this study is to characterize rainy events in central Africa. We use an original database of half-hourly rainfall recorded at 14 rain gauges, which span different climates across CA. The research questions we seek to answer are as follows: (i) What are the characteristics of local rainfall events in terms of amounts, duration, mean, and maximum intensity? (ii) Can we define different types of events according to these characteristics? (iii) What is the accuracy of Integrated Multi-satellitE Retrievals for Global Precipitation Measurement (GPM) (IMERG), a frequently used state-of-the-art satellite estimate of subdaily rainfall, at detecting rainfall events recorded at rain gauges? (iv) What can we infer about the spatial scale and the space–time evolution of rainy events from IMERG?

This paper is organized as follows: section 2 describes the datasets and the methods implemented to characterize the rainfall events; section 3 is devoted to the presentation of the results; Section 4 closes the paper with a summary and the main conclusions.

2. Data and methods

a. Datasets

1) HALF-HOURLY DATA FROM RAIN GAUGES

The original rainfall database includes 30-min rainfall amounts from 14 automatic rain gauges distributed throughout Cameroon, Gabon, Republic of Congo (RoC), and Democratic Republic of Congo (DRC). Figure 1 illustrates the spatial distribution of the rain gauges superimposed onto the topography. The spatial distribution of the rain gauges is uneven, with most stations in Cameroon (6 out of 14), especially in the vicinity of Yaoundé. However, they document four out of the six ecoclimatic regions depicted in Philippon et al. (2019). The recording period varies among rain gauges depending not only on the installation date but also on the quality of data. The recording period, the number of days available for analysis (with 100% availability of 30-min intervals), and the number of rainy or "wet" events (WE) at each rain gauge are presented in Table 1, along with the coordinates of the station (and ecoclimatic region as defined in Philippon et al. 2019).
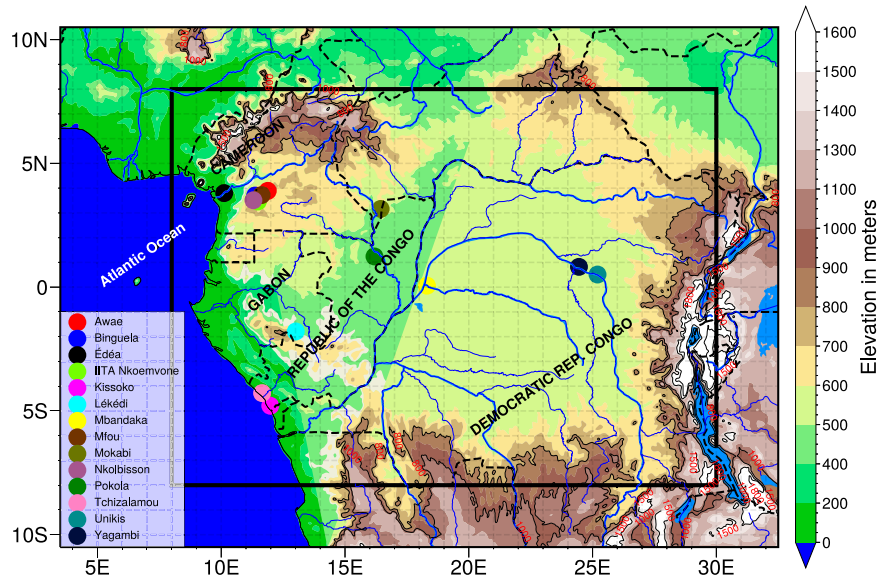
FIG. 1. Spatial distribution of the 14 rain gauges (with their name listed to the left) superimposed on the topographical map [m, from Global 30 arc s elevation dataset (GTOPO30)] for the study region (black rectangle). The main rivers and lakes that cross the region are represented in blue.

These rain gauges were sourced from various ecoclimatic observatories listed below:

1) "Lékédi," in southeast Gabon, was set up in 2012 in the Lékédi Natural Park by Centre National de la Recherche Scientifique (CNRS) in the framework of the Mandrillus project. Rainfall is collected by a DAVIS Vantage Pro tipping-bucket automatic rain gauge at a 30-min resolution and a bucket size of 0.1 mm (i.e., the amount of rain accumulated during the past 30 min).

2) "Nkolbisson," in Cameroon, was set up in January 2009 by the Institut de Recherche Agricole pour le Développement (IRAD). The material and the recording time resolution are the same as at Lékédi.

3) "Pokola" and "Mokabi" in northern RoC were set up by Centre de coopération internationale en recherche agronomique pour le développement (CIRAD) and Institut des Géosciences de l'Environnement (IGE) in March 2016 within two timber forest plots in the framework of the Dynamics of African Forests (DynAfFor) project. For both stations, rainfall data are acquired by a Young tipping-bucket automatic rain gauge at a 15-min resolution and a bucket size of 0.1 mm.

4) "Kissoko" and "Tchizalamou" located in south RoC were, respectively, set up in 2004 and 2006 within the framework of the fonctionnement des écosystèmes forestiers (F-ORE-T) observatory. Rainfall data from both stations were acquired using ARG100 tipping-bucket automatic rain gauges with a 30-min resolution and a bucket size of 0.2 mm.

5) The last eight stations were set up by the Trans-African Hydrometeorological Observatory (TAHMO). TAHMO's aim is to tackle the issue of sparse rain gauge networks in sub-Saharan Africa by installing a network of ~20 000 low-cost hydrometeorological stations (one every 30 km; van de Giesen et al. 2014), which will counteract the decreasing trend of available measuring stations (Schunke et al. 2021). TAHMO's stations are based on the ATMOS 41 model manufactured by METER (https://www.metergroup.com/en/meter-environment/products/atmos-41-weather-station). We extracted data at a 15-min resolution from the eight TAHMO rain gauging stations in central Africa, five are located in Cameroon (Awae, Edéa, IITA Mbalmayo, Binguela, and Mfou) and three in DRC (Mbandaka, Unikis, and Yangambi). Note that TAHMO provides a few other stations for the region. However, we kept only those who offer at least 3 months of data.

Before quality control, a series of pretreatments were applied. Most states in the study area are 1 h ahead of coordinated universal time (UTC) except for eastern DRC, which is 2 h ahead. In addition, TAHMO stations provide data in UTC, and the remainder of the stations provide data in local time (LT). When working with IMERG, all the station records in LT are converted to UTC; otherwise, all records are either converted to or kept in LT. Data from Pokola, Mokabi, and TAHMO stations, at a 15-min resolution, are passed to the 30-min resolution to match the coarsest resolution of Lékédi, Nkolbisson, Kissoko, and Tchizamalou. Missing values are replaced by not a number (NaN). Most projects carry out regular quality screening of their data. TAHMO applies quality screening processes that include not only cross-calibration between sensors and comparisons between nearby stations but also a qualitative intercomparison with satellite observations (van de Giesen et al. 2014; Macharia et al. 2022). Schunke et al. (2021) investigated the quality of TAHMO data for Burkina

TABLE 1. List of stations with their location, eco-climatic region, the mean annual rainfall from IMERG, the recording period, the number of days with records, and the number of WEs extracted.

Station name	Country	Ecoclimatic region	Location (lat, lon)	The mean annual rainfall from IMERG (2001–20) (mm)	Recording period	No. of available days	No. of WE
Awae	Cameroon	Cameroon	3.89°, 11.88°	1605	24 Jan 2020–31 Dec 2020	342	117
Binguela	Cameroon	Cameroon	3.7°, 11.37°	1660	19 Sep 2018–31 Dec 2020	834	440
Édéa	Cameroon	Cameroon	3.80°, 10.12°	2319	29 Jan 2020–31 Dec 2020	337	114
IITA Nkoemvone	Cameroon	Cameroon	3.46°, 11.48°	1603	30 Jul 2020–31 Dec 2020	154	138
Kissoko	RoC	SW Gabon	−4.79°, 11.98°	1325	25 Mar 2004–16 Jun 2006	812	713
Lékédi	Gabon	SW Gabon	−1.79°, 13.01°	2003	19 Mar 2012–31 Dec 2013, 1 Jan 2016–7 Dec 2019	2088	1649
Mbandaka	DRC	North DRC	0.06°, 18.31°	2044	16 Nov 2019–31 Dec 2020	411	244
Mfou	Cameroon	Cameroon	3.72°, 11.6°	1767	18 Sep 2018–31 Dec 2020	835	513
Mokabi	RoC	W&E margins	3.16°, 16.44°	1575	5 Mar 2016–31 Dec 2020	1762	1989
Nkolbisson	Cameroon	Cameroon	3.52°, 11.52°	1609	26 Jan 2009–29 Jul 2011	914	768
Pokola	RoC	W&E margins	1.24°, 16.19°	1683	8 Mar 2016–31 Dec 2020	1759	1625
Tchizalamou	RoC	SW Gabon	−4.28°, 11.65°	1396	1 Jan 2006–3 Dec 2009	1432	1397
Unikis	DRC	North DRC	0.51°, 25.20°	1834	17 Mar 2018–3 Aug 2018	139	57
Yangambi	DRC	North DRC	0.82°, 24.45°	1958	14 Mar 2018–31 Dec 2020	1023	332
Total						12 842	10 096

Faso and concluded that it potentially offers a reliable and cost-efficient solution for applications in hydrometeorology. As part of flux network (FLUXNET), data issued from the F-ORE-T observatory have also been subjected to rigorous quality checks. Data for Lékédi, Pokola, and Mokabi undergo automated and supervised data inspections to detect and rule out erroneous records, especially those associated with bucket blocking. We applied to all the stations an additional temporal consistency check, which filters out nonzero constant values lower than 0.3 mm for at least 3 consecutive hours. That generally happens when the rain gauge is blocked, which results in repeated occurrences of very low amounts. Such sequences are replaced by NaN.

2) HALF-HOURLY RAINFALL ESTIMATES FROM IMERG V6B

The IMERG V6B is the flagship product of a joint mission of the National Aeronautics and Space Administration (NASA) and Japan Aerospace Exploration Agency (JAXA) to estimate surface precipitation over global land and ocean surfaces (Hou et al. 2014). It is the primary level three globally gridded precipitation product from the GPM mission that unifies observations from a network of partner satellites in the GPM constellation (Huffman et al. 2020). In IMERG, rainfall estimates are provided at 0.1° grids every half-hour globally. The IMERG algorithm operates to intercalibrate, interpolate, and merge all satellite microwave precipitation estimates, microwave-calibrated infrared estimates, gauge observations, and other data from potential sensors from the TRMM and GPM eras. IMERG provides a variety of rainfall estimates such as "early," "late," and "final" runs to accommodate different user requirements for latency and accuracy. As in Freitas et al. (2020), Maranan et al. (2020), and Moron et al. (2021), we used here the "final run" because it is considered as the most accurate one among the three runs, and it is also the most widely used in climate studies (O et al. 2017; Maranan et al. 2020; Freitas et al. 2020; Moron et al. 2021). It shall be mentioned, however, that the near-real-time products of TRMM and GPM performed better in cases of the most extreme daily rainfall events in Uganda (Ageet et al. 2022) and the western Rift mountains (Monsieurs et al. 2018), i.e., here, the monthly gauge calibration worsened the performance.

IMERG final run product includes two precipitation variables, namely, the microwave-infrared estimates without gauge adjustment (IMERG_uncal) and the calibrated (IMERG_cal) product based on the Global Precipitation Climatology Centre (GPCC) monthly gauge analysis (Schneider et al. 2008). We used IMERG_cal rainfall in this study. Note that none of the 14 stations worked are used to calibrate IMERG. IMERG_cal data are updated in near–real time with a minimum latency of 3.5 months after observation time and are free for download from NASA (https://gpm.nasa.gov/data/directory).

b. Methods

1) WET EVENT DEFINITION AND CHARACTERIZATION

In this study, a WE is defined as the consecutive (or isolated) half-hours that record at least 0.1 mm. To characterize the WEs, the following metrics are calculated: their duration from their start to their end, their total rainfall amount (the total accumulated rainfall within duration), their maximum (highest half-hourly amount), and mean intensity [i.e., total rainfall amount divided by duration in mm $(30 \text{ min})^{-1}$]. The total number of events and the interevent duration (i.e., the time between two consecutive wet events) are also computed. Five of the six Cameroonian weather stations are very close to each other, questioning the probability of counting the same wet event several times. Note first that most stations only have 1 year (2020) of data in common. Then, we computed the probability that a rainfall event occurred simultaneously at two stations at the same time. Let t_a be the WE onset time at gauge a and t_b be the WE onset time at gauge b (Upton 2002). The difference between these times is denoted $T = t_a - t_b$. This lag was calculated with Binguela as the reference ("b") as it is the westernmost station of the five stations considered. We found only 50 events with $T = 0$ min (i.e., a WE simultaneously recorded at two stations out of five), 42 events with $T = 30$ min and 28 events with $T = 60$ min out of 2090 wet events extracted in total for these six stations. So, WEs at the Camerooneese stations may be considered as mostly independent of each other. Before defining a WE, a sensitivity test was conducted using the 0.2-mm thresholds because two out of the 14 rain gauges (Kissoko and Tchizalamou) have a measurement accuracy of 0.2 mm, while the remainder have an accuracy of 0.1 mm. We observed that by using the threshold of 0.2 mm, the number of events decreases from 10 096 to 7598 and some events are artificially split into two events. If we consider the threshold of 0.1 mm, the longest event has a duration of 36 h, while if we consider the threshold of 0.2 mm, the longest event has a duration of 24 h. We also observed that rainfall events with a rainfall amount between ≥0.1 and <0.2 mm contributed 534 mm or 1.11% of the total rainfall amount.

2) EXTRACTION OF WET EVENT TYPES FROM RAIN GAUGE DATA ACCORDING TO INTENSITY AND DURATION

To assess whether WEs show distinct features in terms of duration and intensity and to extract specific WE type, we applied a k-means dynamical clustering on the whole set of WEs (Moron et al. 2021, 2023). The k-means technique is a partitioning method that classifies each dataset into one of the k groups according to a distance measure. In other words, k-means clustering targets to group data points so that the within-cluster variance is small and the intercluster variance is large (Wilks 2011).

The 10 096 WEs identified were concatenated into a matrix where each row corresponds to a given WE and the columns correspond to half-hourly rainfall amounts from the WE onset time to the WE end. Half-hourly rainfall amounts were square-rooted before applying the k-means in order to reduce the skewness of data and then normalized to zero mean for each half-hourly time step from the WE onset time. We used the elbow criterion and the silhouette coefficient to select the appropriate number of clusters. The elbow method (Thorndike 1953) is a visual method; it starts with $k = 2$, k increasing by 1 at each step, and calculates the sum of squared errors (SSE) of each classification. Then, the SSE curve is plotted with the number of clusters k. The location of a bend (knee) in the curve is generally considered as the indicator of the appropriate number of clusters. The silhouette coefficient has a range of $[-1, 1]$. A value of $+1$ indicates that the sample is far away from the neighboring clusters, so the classification is good. A value of 0 indicates that the sample is on or very close to the decision boundary between two neighboring clusters, while negative values indicate that the sample might have been assigned to the wrong clusters (Xing et al. 2018; Carvalho et al. 2016). We ran the k-means with 1000 iterations each time and values of k ranging from 2 to 9. We finally retained $k = 6$ as the chosen number of clusters from the elbow criterion and silhouette coefficient (Fig. S1 in the online supplemental material). The six types of WEs are referred to as "storm types" (STs) hereafter.

3) ASSESSMENT OF IMERG PERFORMANCE AT DETECTING WET EVENTS

IMERG data are used to assess the spatial scale/footprint of the storm types and their space–time propagation during their lifespan. Before exploring these features for the six STs through IMERG, it is important to assess the skill of the latter at detecting WEs first. We extracted the IMERG grid point collocated with each rain gauge (Table 1; e.g., Maranan et al. 2020; Ageet et al. 2022; Moron et al. 2021, 2023). We recognize that this assumption is not always reasonable since a 0.1° grid box cannot be strictly representative of stations, especially at short time scales when spatial variability can be substantial. We cannot really assess the spatial variations at short distances since our 14 stations are located in different 0.1° grid boxes. To be consistent with the accuracy of rain gauges, which are 0.1 mm $(30 \text{ min})^{-1}$, the same threshold is adopted to define a wet half-hour in IMERG. It should be noted that remote sensing datasets used in IMERG are not direct measures of instantaneous rainfall at the ground level. Note that a lag was applied to match the 30-min periods exactly due to the way the time stamps were assigned to the 30-min rainfall accumulations in the satellite and rainfall data (You et al. 2019). IMERG's skill and accuracy were assessed against rain gauges through a series of statistical measures: hit (HR) when both

rain gauges and IMERG report a wet half-hour, misses (M) when a wet half-hour is reported in rain gauges only, false alarm (F) when a wet half-hour is reported in IMERG only, and correct negative (C) when rain gauges and IMERG both report a "dry" half-hour. From HR, M, F, and C, we calculated four scores that evaluate IMERG performance to identify rain occurrence: the probability of detection (POD), probability of false alarms (POFAs), bias in detection (BID), and the Heidke skill score (HSS). These metrics have been widely used (e.g., Tang et al. 2016; Dezfuli et al. 2017; Camberlin et al. 2020; Freitas et al. 2020; Maranan et al. 2020; Ageet et al. 2022; Macharia et al. 2022) and are described in detail by Wilks (2011)

$$\text{POD} = \frac{\text{HR}}{\text{HR} + M}, \tag{1}$$

$$\text{BID} = \frac{\text{HR} + F}{\text{HR} + M}, \tag{2}$$

$$\text{POFA} = \frac{F}{\text{HR} + F}, \tag{3}$$

$$\text{HR} \frac{2(C \times \text{HR} - F \times M)}{(\text{HR} + F)(F + C) + (\text{HR} + M)(M + C)}. \tag{4}$$

POD quantifies the ability of IMERG to correctly detect rainfall recorded by rain gauges; its value varies from 0 to 1 (and 1 is a perfect score). POFA is the fraction of false alarms relative to all rainfall occurrences in IMERG. BID indicates whether IMERG tends to overestimate (BID > 1) or underestimate (BID < 1) the rainfall frequency. HSS quantifies IMERG's skill in detecting precipitation while incorporating the effect of matches due to random chance, where a perfect score is 1 and HSS > 0 (<0) is better (worse) than random probability. Several other metrics have also been computed to assess the deviation of rain rates in IMERG (e.g., Maranan et al. 2020; Tan et al. 2016; Tan and Duan 2017). These metrics include mean error (ME), mean absolute error (MAE), and their normalized counterparts normalized mean error (NME) and normalized mean absolute error (NMAE). They are calculated as follows

$$\text{ME} = \frac{1}{N} \sum_{i=1} (\text{IMERG}_i - \text{RG}_i), \tag{5}$$

$$\text{NME} = \frac{\frac{1}{N} \sum_{i=1} (\text{IMERG}_i - \text{RG}_i)}{\frac{1}{N} \sum_{i=1} (\text{RG}_i)}, \tag{6}$$

$$\text{MAE} = \frac{1}{N} \sum_{i=1} |\text{IMERG}_i - \text{RG}_i|, \tag{7}$$

$$\text{NMAE} = \frac{\frac{1}{N} \sum_{i=1} |\text{IMERG}_i - \text{RG}_i|}{\frac{1}{N} \sum_{i=1} (\text{RG}_i)}, \tag{8}$$

where RGs_i and IMERG_i represent a pair of rain gauge and IMERG half-hourly rainfall and N is the number of samples.

All error measures are perfect if 0. MAE quantifies the overall error magnitude, and ME measures the bias and its direction.

4) CHARACTERIZATION OF THE SPATIAL FOOTPRINT AND THE SPACE–TIME EVOLUTION OF THE WET EVENT TYPES FROM IMERG

The spatial scale of the WE types was estimated by compositing IMERG rainfall fields of all observed WEs for each storm type. The rainfall field associated with each WE was extracted over an area of 14° latitude × 14° longitude (i.e., roughly a surface of about 2 418 025 km^2) centered on the associated rain gauge. This window size allows us to capture in theory a wide range of rain-bearing systems, from isolated thunderstorms to mesoscale convective systems. Then, all the rainfall fields were averaged for each storm type. The typical spatiotemporal evolutions of the WEs, referred to as "spatial types" hereafter, were also documented, thanks to IMERG and a k-means clustering. Camberlin et al. (2024) found that the direction rain cells travel in changes with the seasons. They move in a southwesterly direction in January and a northwesterly direction in July. As for the analysis of the spatial footprint of the STs, IMERG fields were extracted for each WE over an area of 14° latitude × 14° longitude centered on each rain gauge and from the WEs onset time up to 12 h before. Six time lags were sampled: t0 − 12 h, t0 − 9 h, t0 − 6 h, t0 − 4 h, t0 − 2 h, and t0, where "t0" is the event onset time. We ended up with a matrix of 10 096 rows (the number of WEs) and 11 7600 columns (6 time lags × 14° latitude × 14° longitude). Data were preprocessed before applying the k-means. First, they were standardized by subtracting the corresponding average rainfall from each time lag and spatial location. We did not normalize to unit variance so that more weight is given to the wettest time windows and locations (Moron et al. 2021). Then, we reduced the matrix dimensions and filtered out noise by applying a principal component analysis (PCA; Wilks 2011). PCA allows a decomposition of a spatiotemporal rainfall field $Y(t, s)$ into spatial patterns $S_i(s)$ (s being the spatial dimensions with 6 time lags) and its associated temporal indices $T_i(t)$ (t being the time steps from the event onset time). PCA is based on the following equation:

$$Y(t, s) = \sum_{k=1}^{n} T_i(t) \times S_i(s). \tag{9}$$

PCA provides a new set of uncorrelated linear combinations of the original field [principal components (PCs)] that captures its original variance. We kept 75% of the total variance. The PC matrix was then subjected to the k-means clustering with 1000 iterations and k varying from 2 to 6. We finally retained four clusters (Fig. S2) as the ideal k number according to the same statistical scores as discussed above and the physical interpretation of the spatial types obtained. To further characterize these spatial types, we also composited the fields of rainfall for time lags up to 12 h after the WE onset time, as well as the associated fields of rainfall probability of occurrence.

The relationships between the storm types and the spatial types were evaluated by synthesizing both classifications into a contingency table. The chi-squared test of independence (χ^2) was used to check whether both classifications are likely to be related or not. The chi-squared distribution, a family of continuous probability distributions, is used to calculate the test statistic. This statistic is found by taking the squared difference between observed and expected data values and then dividing that difference by the expected values using the formula

$$\chi^2 = \sum_{ij} [O_{ij} - E(n_{ij})]^2 / E(n_{ij}), \tag{10}$$

where O_{ij} is the observed value and $E(n_{ij}) = (r_i \times c_j)/N$ is the expected value. With N being the grand total, r_i is row i and c_j is column j. The P value is used to determine if the observed difference between actual and expected data is statistically significant. In addition, the relationships between each storm type and each spatial type are evaluated by computing the anomalous probability of occurrence, which is the difference between expected and observed values. It is defined as

$$P_{ij} = \{[O_{ij} - E(n_{ij})]/E(n_{ij})\} \times 100. \tag{11}$$

The 95% significance level of P_{ij} was evaluated using the nonparametric bootstraps. The nonparametric bootstrap procedure is very similar to a Monte Carlo test (Livezey and Chen 1983). The main difference between them is that in a Monte Carlo test, the random data are generated by a random number generator for a specific probability distribution (such as normal). In contrast, in the nonparametric bootstrap, the random data are generated by resampling from the original data, and the resulting sample of estimates often forms a Gaussian distribution. We randomly permuted both classifications 100 times, and then, P_{ij} of the sample was computed and subjected to confidence intervals.

3. Results

a. Duration, amount, and intensity of wet events recorded at stations

This section depicts the main characteristics of the WEs recorded at stations in terms of mean duration, amount, intensity, and frequency.

The mean seasonal cycles of rainfall amount from the IMERG grid point collocated with each rain gauge are shown in Fig. 2. The rain gauges over the study area can be grouped into five subregions based on the main rainfall regime documented by Dezfuli et al. (2017) and Camberlin et al. (2019). Cameroon (Figs. 2a–f), northern Congo–Brazzaville (Fig. 2g), and Central DRC (Figs. 2h–j) rain gauges have a bimodal rainfall regime with a peak in October and May, more abundant rain in September–November, and a main dry season in December–February (for Cameroon and northern Congo). These peaks are related to the latitudinal migration of the tropical rain belt. Their mean annual rainfall amount ranges from 1603 to 2319 mm according to IMERG. By contrast, Gabon and southern Congo–

Brazzaville rain gauges (Figs. 2k–m) exhibit one long rainy season from October to May, peaking in November and April, and a long dry, almost absolute, dry season from June to August. Mokabi rain gauge (Fig. 2n), closer to the Central African Republic, has a unimodal rainfall regime with a rainy season ranging from March to November and a dry season centered on December–February.

According to the definition of wet events given in section 2b(1), a total of 10 096 WEs were identified out of 12 842 days available, i.e., that one wet event is recorded every 1.2 days. The number of WEs at each rain gauge is also presented in Table 1. Due to differences in the recording periods primarily, and the stations' location secondarily (which affects the length of the dry seasons), the stations of Pokola and Mokabi in the Republic of Congo contribute most to the total number of WEs.

Figure 3a displays the interevent duration of wet events versus rainfall amount. We found that wet events have an average interevent duration of 6 days, but the median is 2 days, indicating that it generally rains several times a week. Figures 3b and 3c show the contributions of events with different durations to the total number of WEs and the total rainfall amount. Regarding the number of WEs (Fig. 3b), there is an exponential-like decrease with increasing durations as already seen in India and Bangladesh (Moron et al. 2021, 2023): short/long WEs are the most/least frequent. Most WEs lasted less than or equal to 6 h (~98%) and a majority (72%) lasted 1 h at maximum. Though the WEs lasting 1 h or less are the most frequent, they are not the main contributors to the total rainfall amount (Fig. 3c): it is the WEs that last 1.5–2 h that contribute the most (22.5%), followed by those lasting 1 h or less (19.8%) and then 2.5–3 h (~15.6%). The analysis of the contribution to the total amount at each rain gauge (not shown) shows that roughly all rain gauges show a similar shape of contribution but with small differences due to the length of the available period.

Figure 4 illustrates first the relationship between (i) WE duration versus WE amount, (ii) mean intensity, and (iii) maximum intensity. We observe that duration is tightly related to the rainfall amount, with a Pearson correlation coefficient of $r = 0.66$ significant at the 95% level (p value < 0.05): the longer the event, the wetter it is (Fig. 4a). There is also a significant but moderate relationship between duration and maximum intensity (Fig. 4c, $r = 0.49$, p value < 0.05), meaning that the longest events tend to have the highest 30-min intensities, which is rather expected from the exponential distribution of rainfall. On the contrary, the mean intensity is more weakly related to duration ($r = 0.2$, p value < 0.05).

b. Typology of wet events according to their intensity and duration

The k-means classification applied to the 10 096 WEs highlights six distinct types of WE, referred to as STs and pictured in Figs. 4–6. Figure 5 displays the temporal evolution of 30-min rainfall amounts for each ST. They are ordered according to their mean duration, from the shortest (ST 1) to the longest (ST 6).
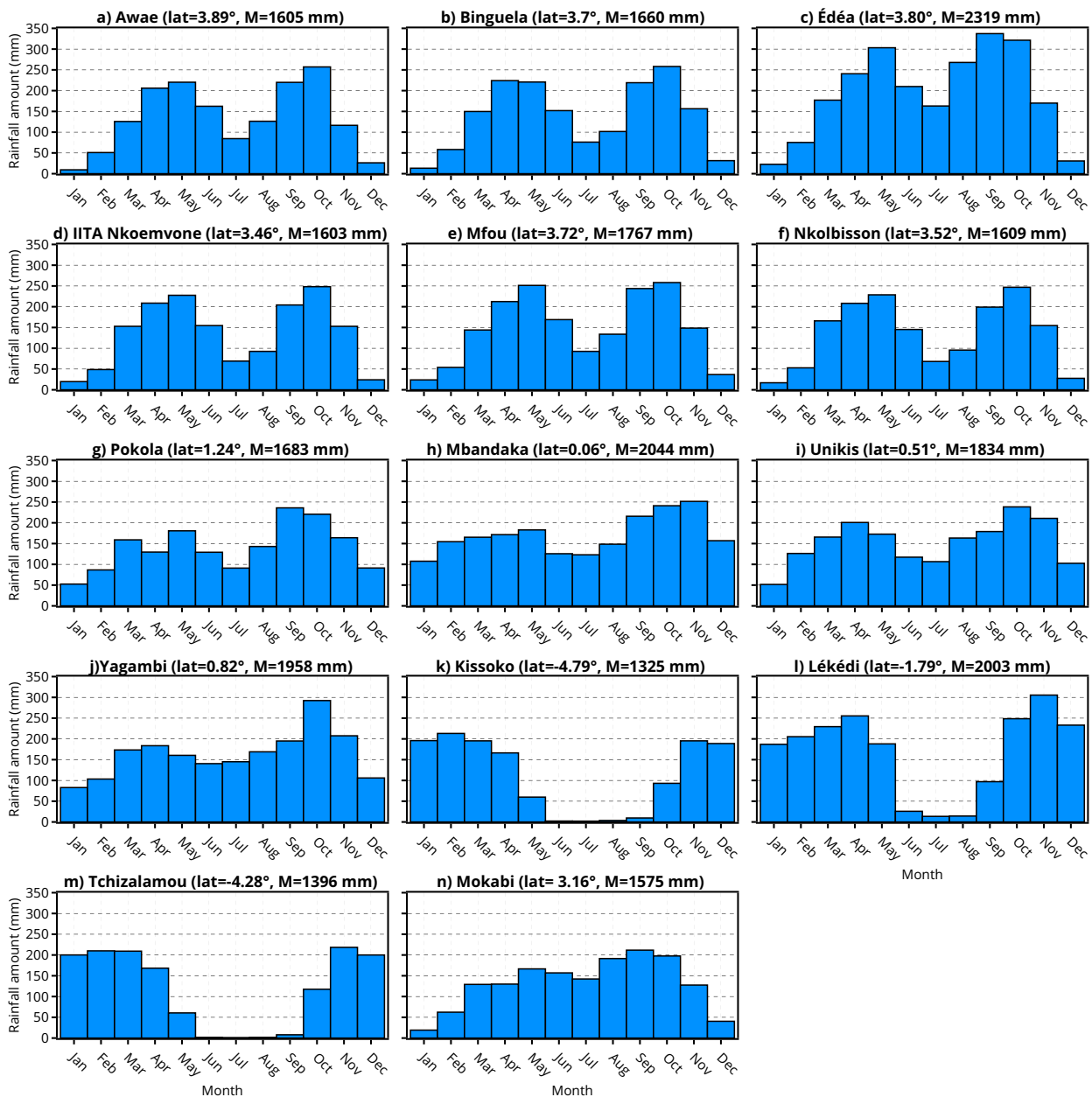
FIG. 2. The mean seasonal cycles of rainfall amount from the IMERG grid point collocated at each rain gauge for the period 2001–20. The gauges are ranked into subregions: (a)–(f) Cameroon; (g) northern Congo–Brazzaville; (h)–(j) central DRC; (k)–(m) southern Gabon and Congo–Brazzaville, and (n) the closer to the Central African Republic.

It is obvious from Figs. 4 and 6 that STs are clearly distinguished by the duration (Figs. 6a–f), total rainfall amount (Fig. 4a), and maximum intensity (Figs. 4c and 6m–r), while the discrimination by mean intensity (Figs. 4b and 6g–l) is more subtle. Figures 6s–x also display the starting hours of WEs, which on average pictures two peaks, in the early morning and in the late afternoon.

ST 1 (Fig. 5a), which comprises about 70% of the WEs, is very short and of very low mean intensity [~0.2 mm (30 min)$^{-1}$, Fig. 4b]. About 95% of WEs comprised in ST 1 lasted less than 90 min and received less than 1.50 mm (Figs. 4a and 6a), explaining that ST 1 contributes to only 6% of the total rainfall. It occurs preferably in the early morning (0400–0700 LT, Fig. 6s).

About 7% of WEs are associated with ST 2 (Fig. 5b), which is sudden (peak of intensity recorded during the first 30 min), short, and intense (Fig. 4b). Its mean intensity [~5 mm (30 min)$^{-1}$] is higher than ST 1, ST 3, and ST 6 but lower than ST 4 and ST 5. Roughly 95% of WEs comprised in ST 2 lasted less than 210 min and received less than 29 mm (Figs. 4a and 6b), contributing on
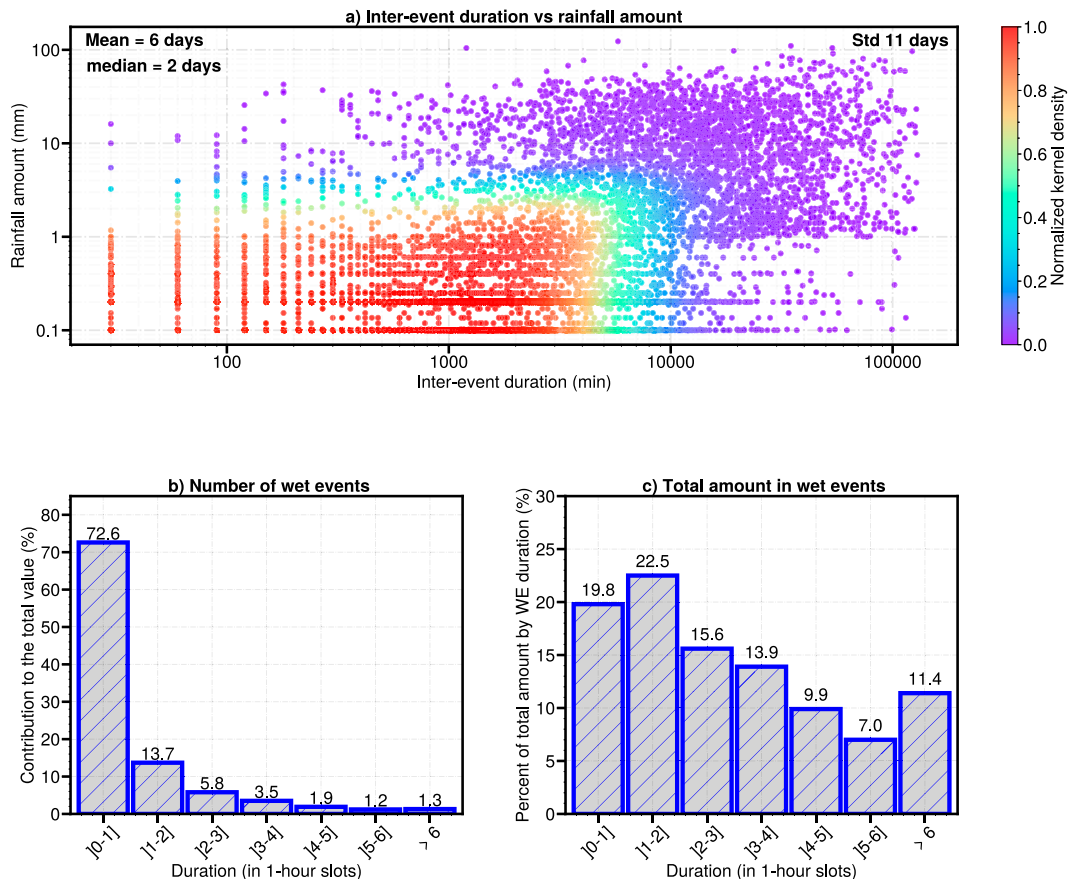
FIG. 3. Interevent duration vs total rainfall amount in logarithmic scale of the 10 096 WEs. (top left) The mean and (top right) standard deviation (Std). Contribution of events with different durations (from 30 min to 6 h and up) to the (b) total number of WEs and (c) total rainfall amount. For (b) and (c) on the x axis, WEs were binned into 1-h intervals.

average to 18% of the total rainfall. ST 2 occurs mainly in the afternoon (1200–1800 LT, Fig. 6t).

ST 3 (Fig. 5c), which accounts for 13.6% of the WEs, is short (95% of events lasted less than 240 min) and of low intensity [~1 mm (30 min)$^{-1}$]. The maximum rainfall intensity is recorded 1 h or more after it starts. It is related to moderate rainfall amounts as the mean contribution to total rainfall equals 13%, and 95% of events received less than 11 mm (Figs. 4a and 6c). It occurs preferably in the afternoon (1200–1800 LT, Fig. 6u).

ST 4 (Fig. 5d) is long (95% of WEs lasted 270 min), intense [~5 mm (30 min)$^{-1}$], but far less frequent (5.3% of the WEs). It is related to high rainfall; 95% of WEs received less than 47 mm (Figs. 4a and 6d), contributing on average to 29% of the total rainfall. As for ST 3, it occurs preferably in the afternoon (1200–2000 LT, Fig. 6v).

ST 5 (Fig. 5e) is long and the most intense [6 mm (30 min)$^{-1}$] but represents only 2% of all WEs. As for ST 3 and intensity peaks 1 h after it starts, followed by a slower decrease of intensities as compared to ST 4. ST 5 is associated with high rainfall amounts and contributes to 20% of total rainfall. About 95% of WEs comprised in ST 5

received less than 87 mm and lasted less than 420 min (Figs. 6e and 4a).

Last, ST 6 (Fig. 5f) is the longest (370 min on average; 95% of WEs lasted less than 600 min) but less intense than ST 2, ST 4, and ST 5 [2 mm (30 min)$^{-1}$]. The maximum intensity peaks 2–3 h after it starts. ST 6 is related to moderate rainfall amounts (95% of WEs received less than 63 mm) and contributes to 13% of total rainfall (Figs. 4a and 6f). It occurs mainly at night (2000–0600 LT, Fig. 6x).

The frequency of occurrence of the six storm types at each station is provided in Fig. 7 as pie charts organized according to the geographic location of the station. To evaluate the significance of the ST frequency at each station, first, the sequence of the frequency of occurrence of STs is randomly permuted 100 times. Second, the mean of the bootstrap estimate is calculated for the randomly permuted 100 sequences of STs. Third, the 95th percentile of the corresponding mean of the bootstrap estimate is identified as the threshold. Finally, the frequency of occurrence of STs is considered statistically significant if the corresponding ST is not less than the identified threshold. It is noteworthy that ST 1 (the shortest and least intense ST) is far more frequent (72%) at the
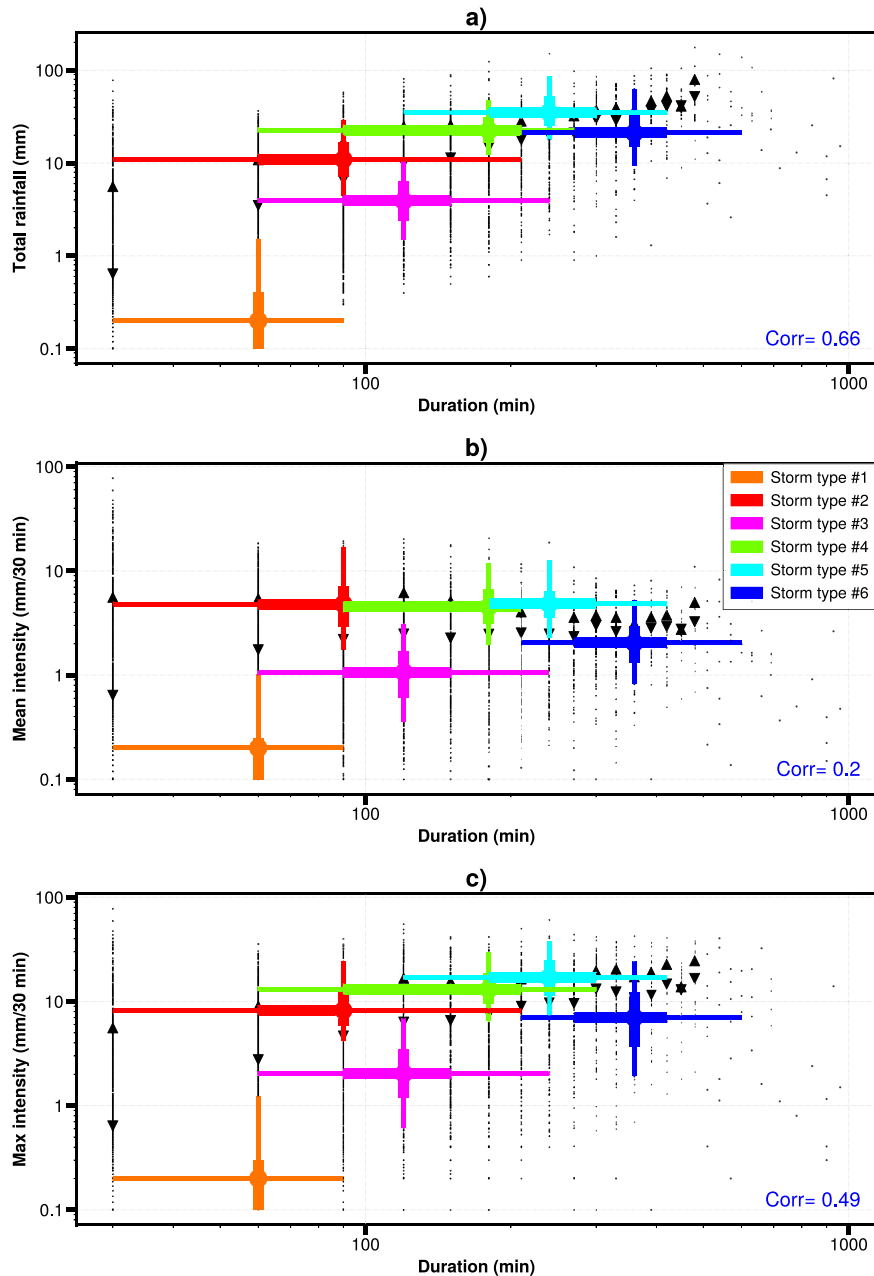
FIG. 4. Scatterplots (black dots) of (a) the total rainfall amount, (b) mean intensity, and (c) maximum intensity (*y* axis, in logarithmic scale) with the duration (*x* axis, 30-min slots) for the 10 096 WEs. The median (colored dots) with the 25th–75th (large colored lines) and 5th–95th (thin colored lines) percentiles are superimposed for the six STs. The upper and lower black triangles indicate two standard deviations and the mean for 30-min duration time steps. The Pearson correlation coefficient with duration is indicated in the lower-right corner of each subpanel.

northeasternmost (Mokabi, Pokola) and southwesternmost (Tchizamalou, Kissoko) stations than at the other ones, and it contributes the least to total rainfall at these stations. This is at the expense of STs 2 and 3, which are less frequent. ST 4, ST 5, and ST 6 are the storm types that contribute most to the total rainfall (Fig. 8). These four stations are the ones which experience the longest and driest dry seasons. It is also interesting to

see that ST 5 (the most intense and second longest ST) seems preferentially recorded at Yangambi and Unikis, the two easternmost stations, at Mbandaka, which is in the "cuvette centrale" of the Congo basin, at Edéa, located in the coastal plain at the western foot of the Mount Cameroon windward slope, and also at Lékédi at the northeast tip of the Batéké plateaux. This could be explained by their location to the west of areas
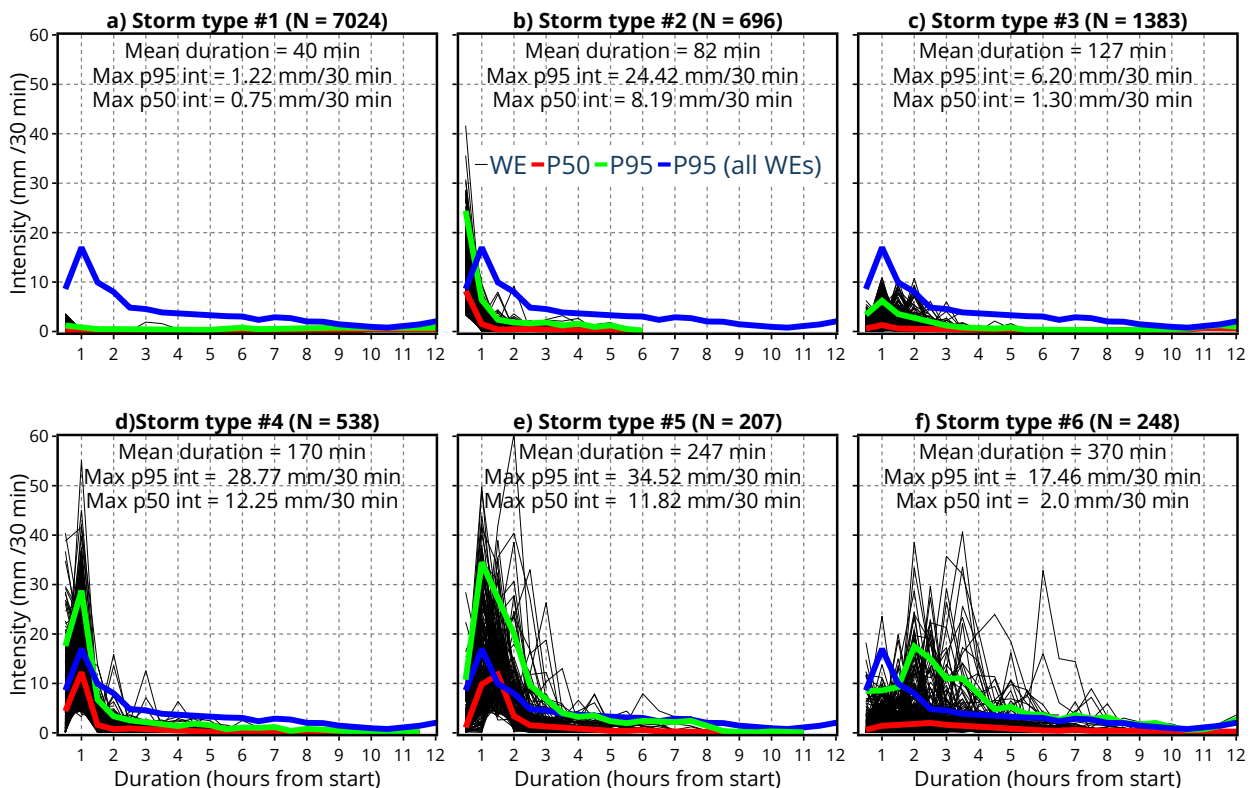
FIG. 5. "Intensity vs. duration" profiles of all the WEs (tiny black line) constituting the (a)–(f) six STs extracted through a *k*-means. The average profile of all the WEs is provided as a blue line. The 50th and 95th percentiles within each ST are provided as red and green lines, respectively. The six STs were rated according to their mean duration. The variable *N* is the number of WEs within each ST. Max p50 int and Max p95 int are the 50th and 95th percentiles of the maximum intensity, respectively.

where convection is preferentially initiated [western slopes of the East African rift and Cameroon Line mountains, the Batéké plateaus; Hartman (2021)] or in the cuvette centrale of the Congo basin, where high evaporation from swamps potentially fuels convection.

c. Evaluation of IMERG

Before exploring the spatial extent of these six storm types through IMERG, it is important to assess the reliability of that latter product first. To our knowledge, the validation of IMERG at subdaily time scale for CA has never been done. The skill of IMERG at detecting wet half-hours whatever the rainfall intensity or for specific ranges of intensity is provided in Table 2. In section B, IMERG performance was computed following the schematic by Maranan et al. (2020) based on true miss, true false alarm, duration +, and duration −. Note that half-hourly periods are based on the rain gauges, due to the fact that IMERG is characterized by an early start and a late end compared to rainfall events observed at rain gauges. This entails that all true false alarms are set to zero. Thus, misses include both true misses and duration −, whereas false alarms contain only duration +. When considering all available time steps whatever the intensity (section A), IMERG displays a high detection capability when it actually rains at the stations (POD = 0.63). However, a large part of the

detections are false (POFA = 0.76), i.e., there is no rain recorded at the stations. Actually, IMERG overestimates the frequency of rainfall (BID > 1), but the HSS value of 0.31 indicates a better skill than pure chance. Regarding specific rainfall intensities (section B), IMERG shows a good performance. POD values are progressively increasing from low to high intensities. The error magnitudes indicate a slight overestimation of rain rates (MAE > 0), and biases indicate a slight underestimation (ME < 0). These results are consistent with Maranan et al. (2020). We conclude that the IMERG skill at detecting rainy events is good enough to be used to examine the spatial footprint of wet events.

d. Spatial scale of the six storm types

After examining the mean characteristics of the six storm types (duration, intensity, amount, and frequency) based on the rain gauge measurements only, it is interesting to investigate their spatial scale thanks to IMERG and thus infer, if possible, the probable meteorological rain-bearing process associated with each storm type (Orlanski 1975; Moron et al. 2021). The right panels of Fig. 9 show kernel density scatterplots between the total rainfall amount (mm) of each WE recorded at the rain gauges versus that at the collocated IMERG grid point for each of the six STs. The number of WEs detected by IMERG (threshold > 0.1 mm) is reported
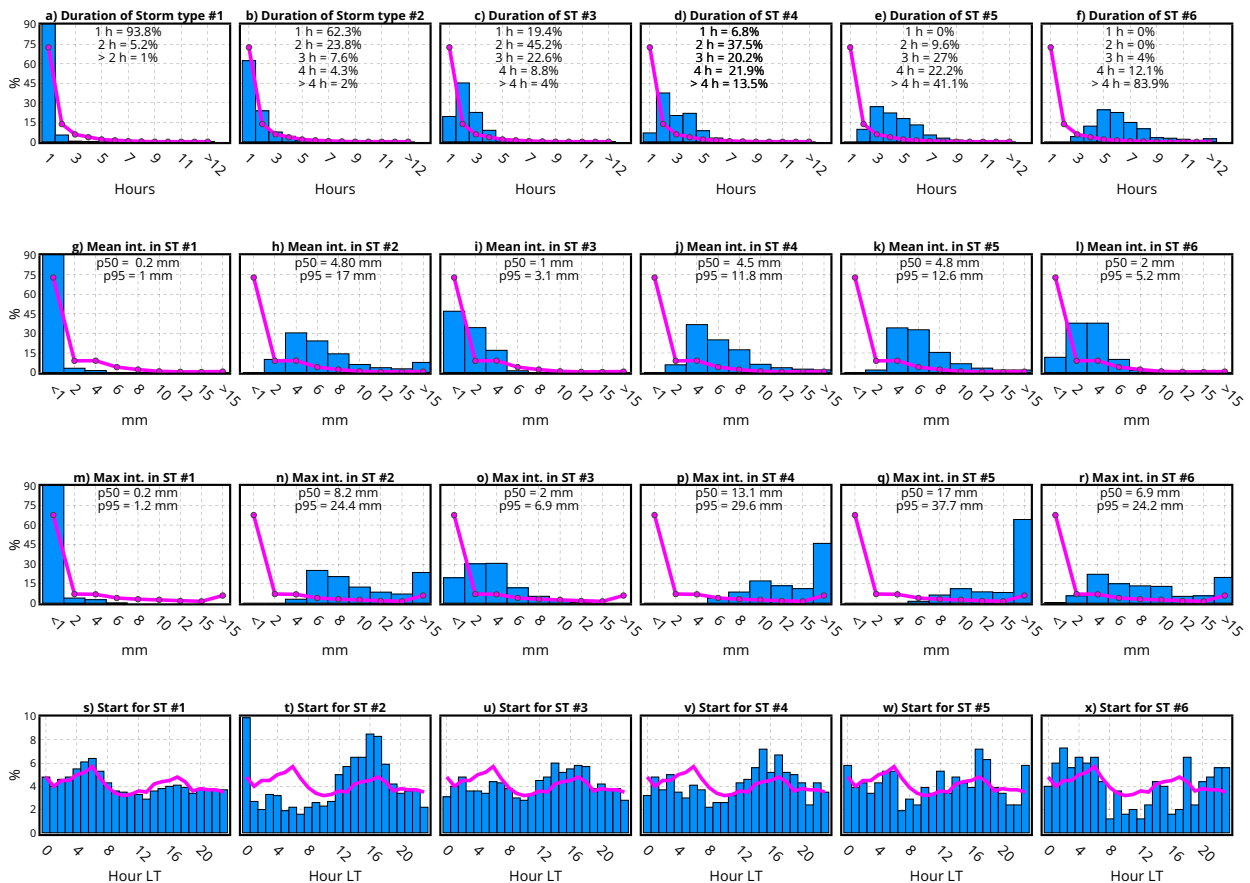
FIG. 6. Distributions for each ST (columns) of the WEs (a)–(f) duration (h), (g)–(l) mean rainfall intensity [mm (30 min)$^{-1}$], (m)–(r) maximum rainfall intensity [mm (30 min)$^{-1}$], and (s)–(x) starting hour (LT). The magenta line is the average of all WEs. The 50th and 95th percentiles are annotated for the mean and max intensities.

in the title of each subpanel, and correlations are also given in the bottom-right corner. We observe that events belonging to ST 1 (the shortest and lightest ST) are the least well detected: solely 2508 wet events out of a total of 7024 identified are seen by IMERG, i.e., approximately 35%. This proportion reaches 62% and 72% for STs 2 and 3, respectively, and more than 83% for STs 4–6 (the longest and rainiest). Overall, the agreement between IMERG and rain gauges is poor, as correlations are mostly below 0.3 (but all significant at the 95% threshold). Nonetheless, values progressively increase from the shortest/lightest to the longest/rainiest STs: the correlation reaches 0.47 for ST 6, pointing to a better detection of long and intense WEs by IMERG. The left panels show the corresponding composite fields of rainfall (for an area of 14° latitude × 14° longitude around the stations) inferred from IMERG for the six storm types. These fields are clearly distinguishable between STs, some depicting an expected circular pattern, with rainfall decreasing from the target station. The diameter of the spatial footprint and total rainfall are concordant with the mean duration of WEs displayed in Fig. 5. This further demonstrates that the size and the total rainfall of WEs are related to the duration. However, it is important to

highlight that IMERG massively overestimates low to moderately intense rainfall (ST 1–2).

ST 1 shows very low total rainfall (<1 mm) over the entire spatial window, indicating that it is of small spatial scale and probably related to local convection. ST 2 and ST 3 display a spatial footprint characterized by moderate rainfall (<3 mm) concentrated within a 2° radius around the target station, with core rainfall reaching 7 and 10 mm, respectively. ST 4 and ST 5 display a larger spatial footprint with high total rainfall (>3 mm) over most of the spatial window analyzed and core rainfall reaching 15 and 25 mm, respectively. ST 5 spatial footprint also pictures an southeast–northwest elongated pattern. Last, ST 6, which includes a few WEs only, has the largest spatial footprint and highest total rainfall amount over the entire spatial window. As for ST 5, it pictures an southeast–northwest spatial extension. Such patterns are probably explained by topographic features as both STs are mainly recorded at the Congolese coastal stations of Lékédi, Kissoko, and Tchizalamou, where convective systems frequently come from the nearby Atlantic and the coastline and Chaillu Mountain range follow a similar orientation. Given their spatial footprint, intensity, and duration, ST 4–6 are probably associated with mesoscale convective systems.
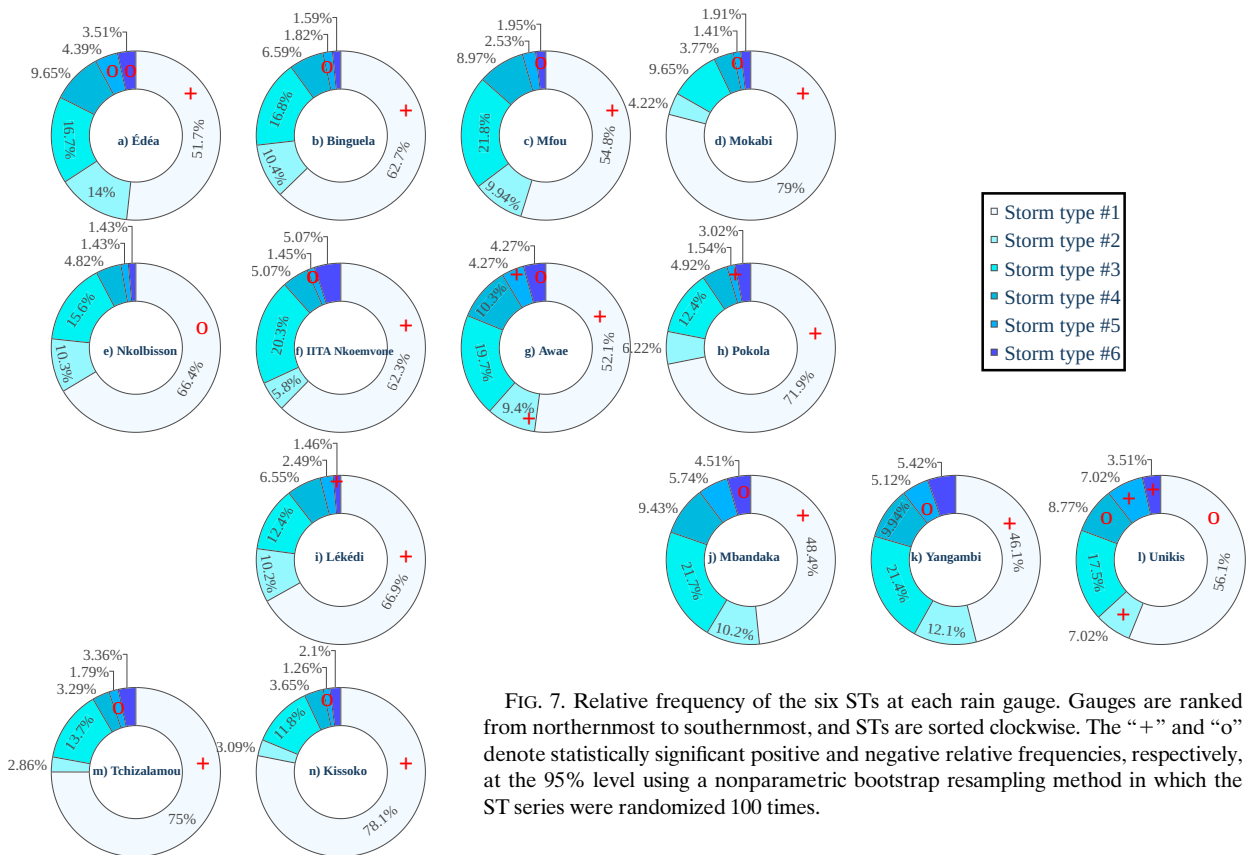
FIG. 7. Relative frequency of the six STs at each rain gauge. Gauges are ranked from northernmost to southernmost, and STs are sorted clockwise. The "+" and "o" denote statistically significant positive and negative relative frequencies, respectively, at the 95% level using a nonparametric bootstrap resampling method in which the ST series were randomized 100 times.

e. Propagative patterns associated with storm type

The previous section has shown that the six storm types extracted have different spatial scales in IMERG. The next point explored is the temporal evolution of their spatial footprints, especially whether the WEs are stationary or propagative, and in the latter case, what is their usual trajectory. To document the space–time evolution of WEs during their lifetime, we used gridded rainfall fields from IMERG again. Following the methodology outlined in section 2b(4), a *k*-means clustering was used to classify WEs according to the associated rainfall field evolution in IMERG. Four spatial types were identified, each one showing quite a distinct rainfall intensity and space–time evolution. They are sorted according to their frequency. The mean rainfall fields from time lags t0 − 12 h–t0 + 12 h for the four spatial types extracted are shown in Figs. 10 and 11 as shadings, while those for the probability of rainfall occurrence are shown as contours. Note that whatever the spatial types, the probability of rainfall occurrence is tightly related to the high rainfall intensities. We observe that the space–time evolution of the mean rainfall field before (Fig. 10) and after (Fig. 11) the WE onset (t0) is nearly symmetrical for each spatial type.

Spatial type 1 (Figs. 10 and 11a–f) is the most frequent, accounting for about two-thirds (~63%) of the total number of WEs. It is characterized by the shortest life cycle and the weakest intensities (<0.3 mm h^{-1}). It is mainly local,

affecting an area of 2° latitude × 2° longitude only. It appears slightly east of the station 4 h before reaching it (t0 − 4 h). At t0 + 6 h, it has moved slightly to the west and has vanished at t0 + 9 h.

Spatial type 2 (Figs. 10 and 11g–i) accounts for about a quarter (~23%) of the total number of events. As compared to the former type, it is more intense, longer, and of larger scale. It is also propagative, moving from east to west. It appears 5° east of the station 12 h before reaching it, with intensities of 0.6 mm h^{-1} affecting an area of 6° latitude × 6° longitude. These intensities increase as it moves westward, to reach 1.6 mm h^{-1} at t0 at the station (Figs. 10g–i). At t0 + 4 h, although it has moved to the west, intensities at the station stay >3 mm h^{-1}. At t0 + 12 h, the station is no longer affected by intense rain.

The spatial types 3 and 4 (Figs. 10 and 11m–r,s–x), which account for ~11% and ~3% of the total number of events, respectively, differ from the first two types. They are associated with far more intense rain, are more persistent, and are nonpropagative. The highest intensities are located to the west of the station, i.e., their core never reaches the station. Their footprint is rather elongated and of broad scale. Spatial type 3 has its rainfall center located ~400 km southwest of the station. Its rainfall intensity reaches 1.6–1.8 mm h^{-1} as early as t0 − 9 h and till t0 + 2 h. Then, it quickly vanishes. Spatial type 4 has its rainfall center located ~500 km northwest of the station. Its rainfall intensity reaches 2.4 mm h^{-1} and up
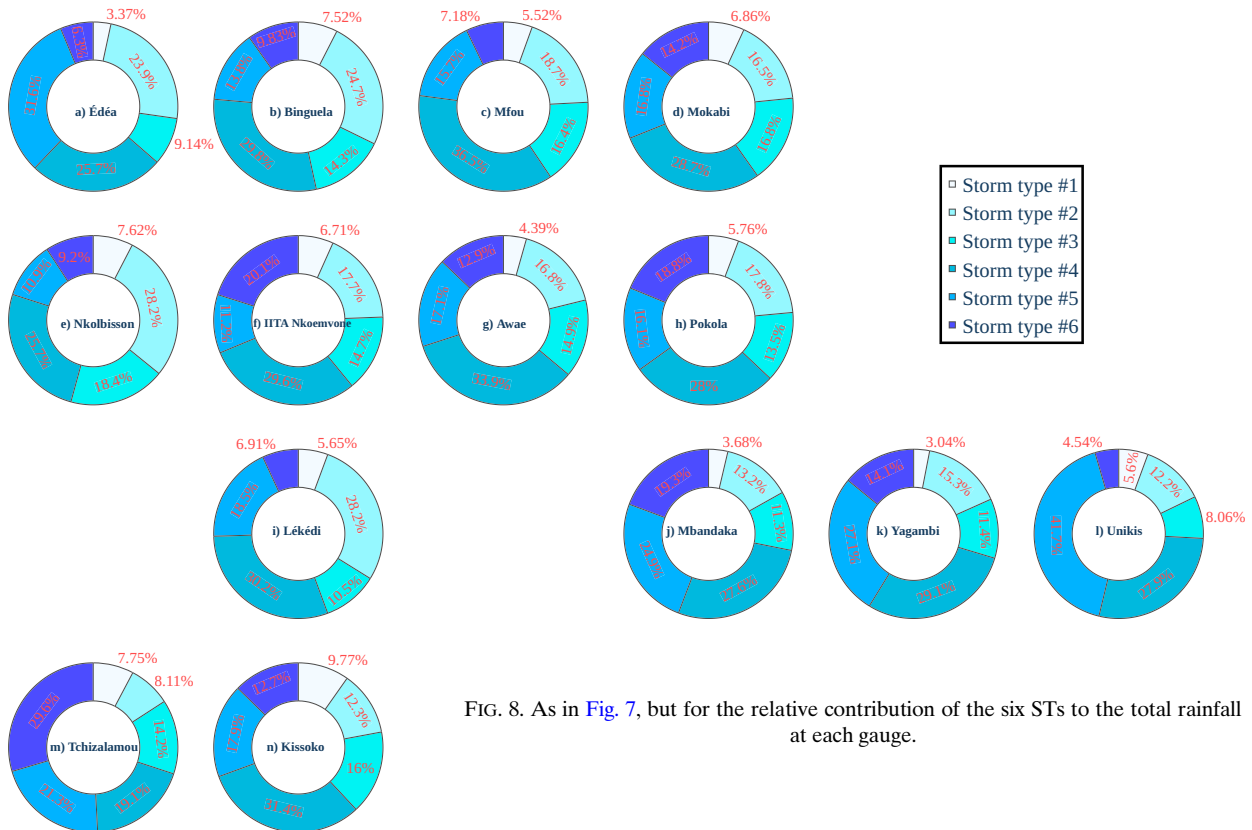
FIG. 8. As in Fig. 7, but for the relative contribution of the six STs to the total rainfall at each gauge.

with intensities above 1.8 mm h^{-1} occupying roughly a 7° latitude × 7° longitude area from t0 − 9 h to t0 + 4 h.

Figures 7 and 12 illustrate the frequency of occurrence of the four spatial types at each station. The northeasternmost (Mokabi) and southwesternmost (Kissoko, Tchizalamou) stations record the largest frequency (>64%) of spatial type 1, which is the one depicting light and short nonpropagative local wet events. These stations also experience the longest dry seasons. Interestingly, Kissoko, Tchizalamou, and Lékédi record the largest frequencies of spatial type 4 (very long and intense stationary event located to the northwest of the station). We hypothesize that this type of event may be related to oceanic modes, which are known to cause longer rainfall over the seas. It is characteristic of thunderstorms that develop over the nearby Atlantic and that move inland due to coastal sea breezes or during the July–August season to the monsoon flux.

Last, Edéa and Mbandaka also stand out with the largest frequencies of spatial type 3 (quite similar to spatial type 4 but located to the southwest of stations). Again, the influence of the nearby Atlantic is expected for Edéa, while for Mbandaka, located in cuvette centrale of the Congo basin, the presence of lakes and swamps may explain this frequency.

To determine whether the association between the two classifications (the six storm types and the four spatial types) is statistically significant, we built a contingency table and computed the chi-square statistic. The result gives $\chi^2 = 30.40$ (with a p value $p = 0.01$), thus suggesting a significant relationship between both classifications. We also computed the anomalous probability of occurrence for each cell of the table, in order to assess whether certain STs are preferably associated with certain spatial types (Fig. 13).

The anomalous probability of occurrence equals −8% between STs 4, 5, and 6 and the spatial type 1, which indicates

TABLE 2. IMERG performance scores computed whatever the rainfall intensity (section A) or for specific intensities (section B).

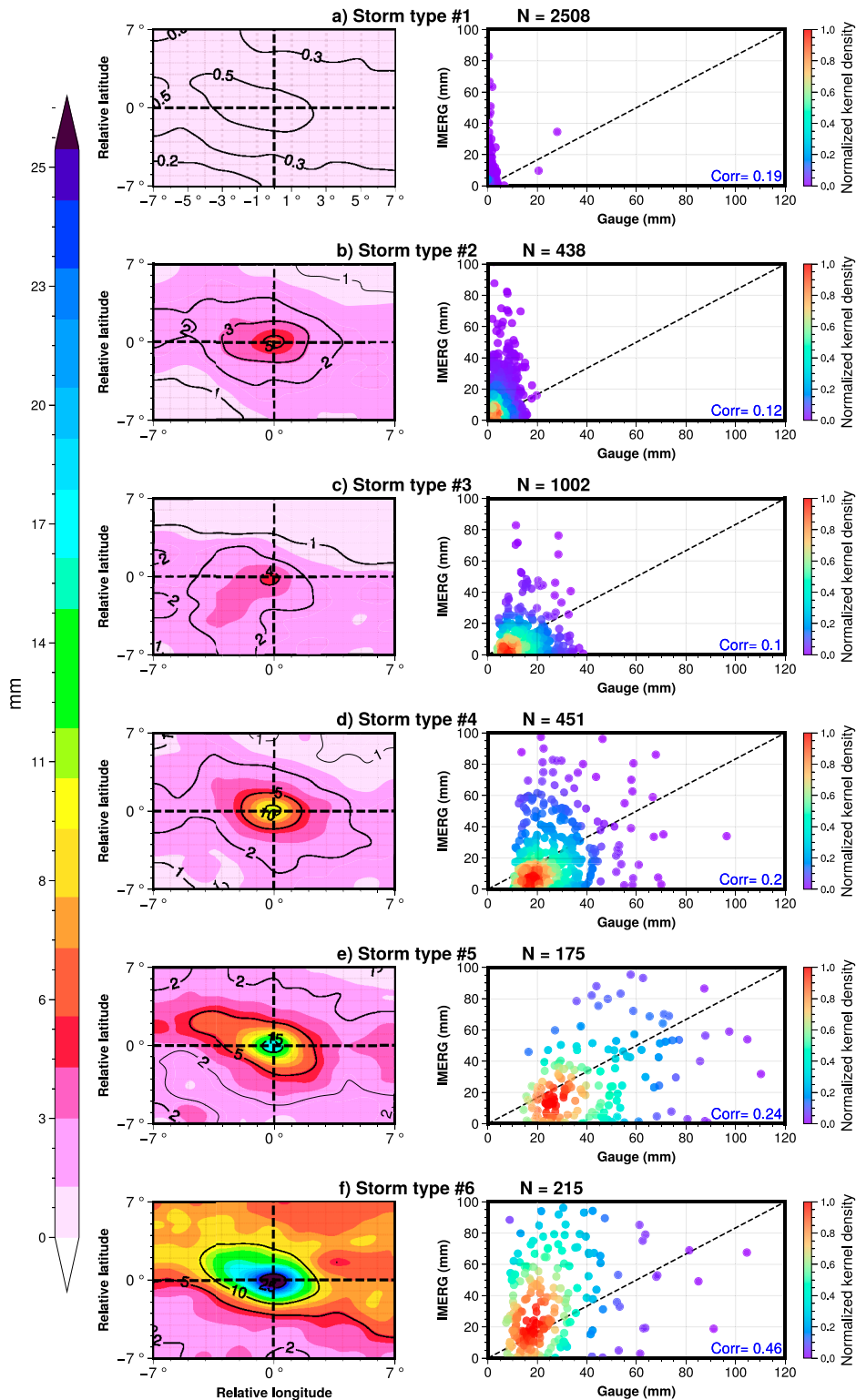| Section	Description	Contingency measures				Rain rate error measures			
		POD	POFA	BID	HSS	ME [mm (30 min)$^{-1}$]	NME	MAE [mm (30 min)$^{-1}$]	NMAE
A	All amounts	0.63	0.76	2.66	0.31	0.01	0.23	0.13	1.70
B	<1 mm (30 min)$^{-1}$	0.56	—	—	—	0.03	3.47	0.03	4.41
	1–5 mm (30 min)$^{-1}$	0.62	—	—	—	0.01	0.36	0.04	1.43
	5–10 mm (30 min)$^{-1}$	0.62	—	—	—	−0.01	−0.11	0.05	1.13
	>10 mm (30 min)$^{-1}$	0.77	—	—	—	0.00	0.17	0.06	1.94

FIG. 9. (left) Composite fields of the total rainfall (mm) for each ST, over a 14° lat × 14° lon window centered on each station. (right) Kernel density scatterplots of the WE rainfall amount recorded at the rain gauge vs the collocated IMERG grid point. The number of WEs detected in IMERG is shown as *N* in the subtitle. The correlation between both datasets is indicated in the bottom-right corner of each panel. All the correlations are significant at the 95% level.
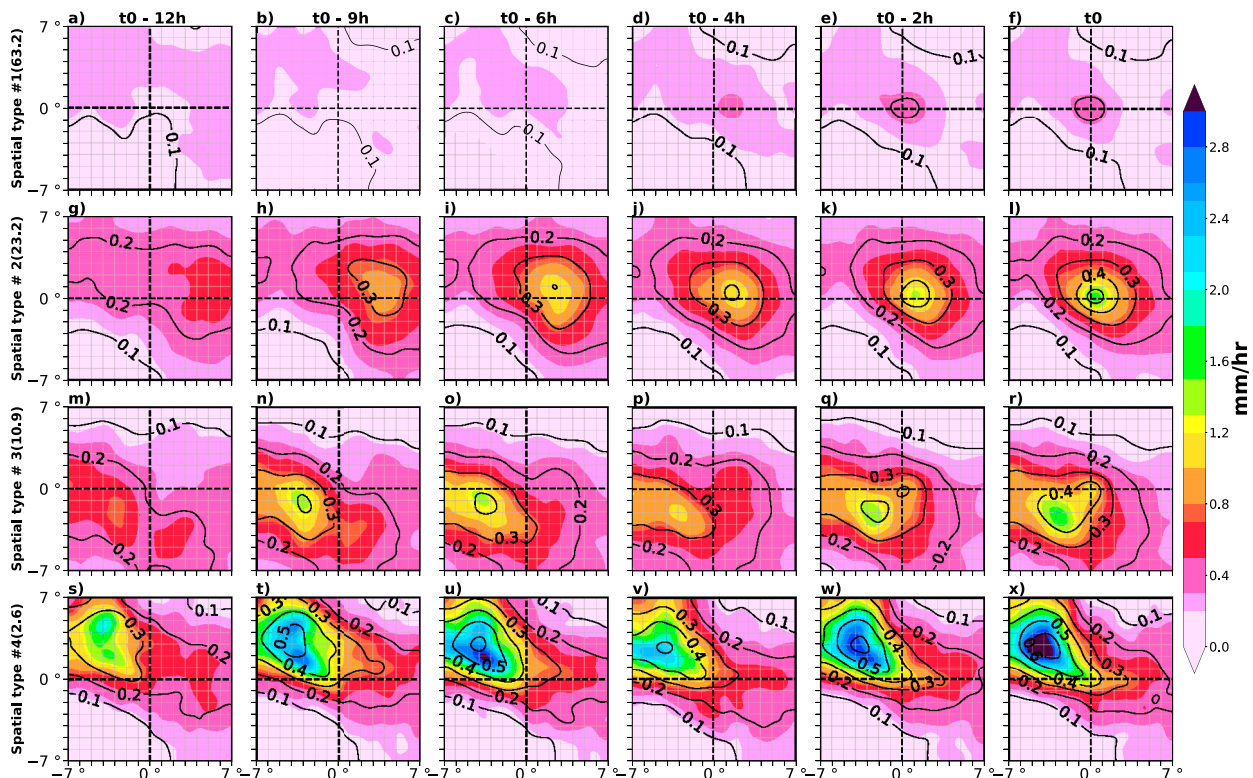
FIG. 10. Composite fields of the mean rainfall intensity (shading, mm hr^{-1}) recorded, for each spatial type (rows), over a 14° lat × 14° lon window centered on each station, from the start of the WE ("t0") to 12 h ("t0 − 12 h," columns) before. Contours are the probability of occurrence of rainfall greater than or equal to 0.1 mm. Values in parentheses on the y axis indicate the proportion (%) of WEs into each spatial type.

that it is unlikely to have very intense and long WEs of small spatial footprint and stationarity. On the contrary, it is more likely (~+10% to 25%) to have ST 4, ST 5, and ST 6 being westward-propagating storms of large scale, i.e., of spatial type 2. ST 5 (which is the most intense ST) is very likely (~70%, nine WEs observed while five expected by chance) to be associated with spatial type 4, which is stationary and has the largest spatial scale and the highest intensities. ST 3, which is long but with light rainfall intensities, is more likely than chance (13%) to be associated with the stationary spatial type 3.

The "+" denote statistically significant positive and negative relative frequencies at the 95% level using a nonparametric bootstrap resampling method in which the STs series were randomized 100 times.

4. Discussion and conclusions

This study is the first to conduct, for central Africa (CA), an analysis of the characteristics of the rainy events at the sub-daily time scale. It relies on (i) an original database of half-hourly rainfall recorded at 14 rain gauges documenting four of the six ecoclimatic regions of CA and (ii) IMERG rainfall estimates. A total of 10 096 wet events (defined as the consecutive or isolated wet half-hours recording more than 0.1 mm) were extracted, and their main characteristics, i.e., duration,

intensity, frequency, and total rainfall, were analyzed. We found that CA is dominated by short duration WEs, as ~72% lasted less than or equal to 1 h. However, these events contribute to only 20% of the total rainfall amount. Instead, it is the WEs that lasted 1 h 30 min–2 h, and that represent only 14% of the total number of WEs, which contribute the most to the total rainfall amount, 22% (Fig. 3).

The analysis of the relationships between duration, total rainfall amount, and intensity (Fig. 4) shows that the total rainfall amount and maximum intensity are positively related to duration, while the mean intensity is almost independent of duration. These results are consistent with Moron et al. (2021, 2023), who observed similar relationships but in different climate regimes and used data at a much coarser time resolution (1–3 h).

To extract typical WE types, the wet events were dynamically clustered according to their duration/intensity profile using the nonhierarchical k-means method. Six storm types (STs) were obtained. Although by construction, they are mostly discretized by their duration and intensity, these STs are also distinguished by their mean and maximum intensity, shape, and spatial extent (Figs. 4–6).

Another feature of rainy events is their space–time evolution, which can also be inferred from IMERG gridded rainfall fields. An additional k-means classification was performed using IMERG to assess the WE spatial scale, and whether they
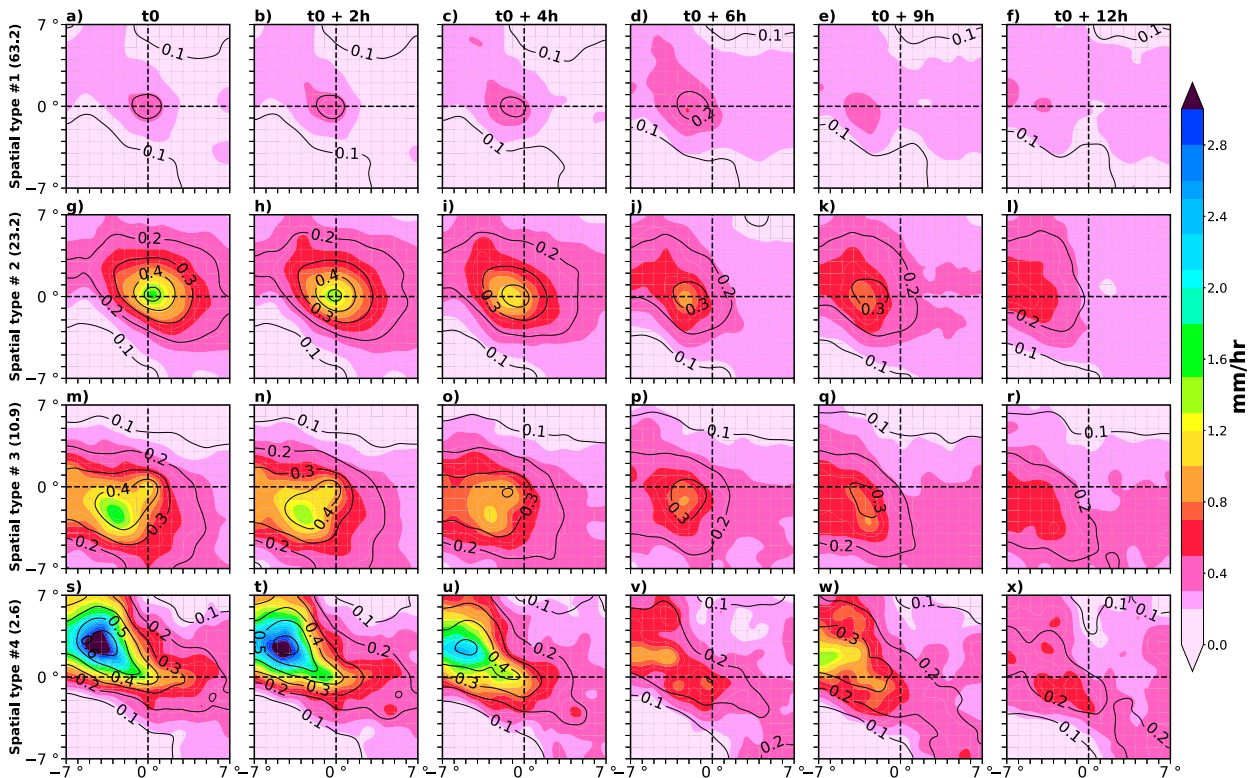
FIG. 11. As in Fig. 10, but up to 12 h after (t0 + 12 h) the WE start.

are stationary or propagating during their lifetime. Four spatial types were extracted, mostly discretized by the evolution, from the WE onset up to 12 h before, of the rainfall field over a 14° × 14° latitude–longitude window around the target station.

Our key findings on rainy event characteristics in central Africa are summarized below:

- The most frequent WEs (70%, ST 1) are characterized by very low rainfall intensity [P50 = 0.2 mm (30 min)$^{-1}$] and, amount, are of very short duration (mean duration < 1 h), and of small spatial scale. However, they contribute to 6% of the total rainfall only. They preferentially start early in the morning and are not associated with any particular spatial type. They are more frequent in the northernmost/southernmost stations and less frequent in the easternmost ones. They are probably related to stratiform rain within small local systems or at the margins of convective systems passing away from the stations (Bulovic et al. 2020; Shige et al. 2013). They pose a major challenge for IMERG as only ~35% of these WEs are correctly detected. This has also been reported in previous studies carried out on other regions and climate regimes (Tan et al. 2016; Dezfuli et al. 2017; O et al. 2017; Maranan et al. 2020; Moron et al. 2021; Bulovic et al. 2020).

- Seven percent of the WEs (ST 2) are sudden and intense (highest mean) but remain brief (mean duration ~1.5 h), with low rainfall amount and moderate spatial scale. This type of WE preferentially starts in the afternoon and is less

frequent in the coastal stations of Congo–Brazzaville. They are moderately well detected by IMERG (62%).

- Thirteen percent of WEs (ST 3) are of short duration, light intensity, low rainfall amount, and moderate spatial scale. They preferentially start in the afternoon and tend to be nonpropagative (more likely associated with spatial type 3). They are well detected by IMERG (72%).

- The long, intense, high rainfall and of large spatial scale WEs (ST 4) typically occur in the afternoon. They contribute to almost 30% of the total rain. They tend to be propagative (preferentially associated with spatial type 2), moving from east to west across the region. They are very well detected by IMERG (82%). They are probably related to mesoscale convective systems.

- The least frequent type of WEs (ST 5, 2%) gathers long and intense WEs, with high rainfall amount and of large spatial scale. These events have no preferential starting hour. They are more likely nonpropagative and form in the west (spatial type 4). They are very well detected by IMERG (83%) and are also probably related to mesoscale convective systems.

- The longest, wettest (but not the most intense), and of largest spatial scale WEs (ST 6) are also rare (3%). They preferentially occur at night and are more likely propagative (associated with spatial type 2). They are probably associated with mesoscale convective systems moving westward over the region (as ST 4) but less active or not strictly under the core of mesoscale convective systems. They are very well detected by IMERG (85%).
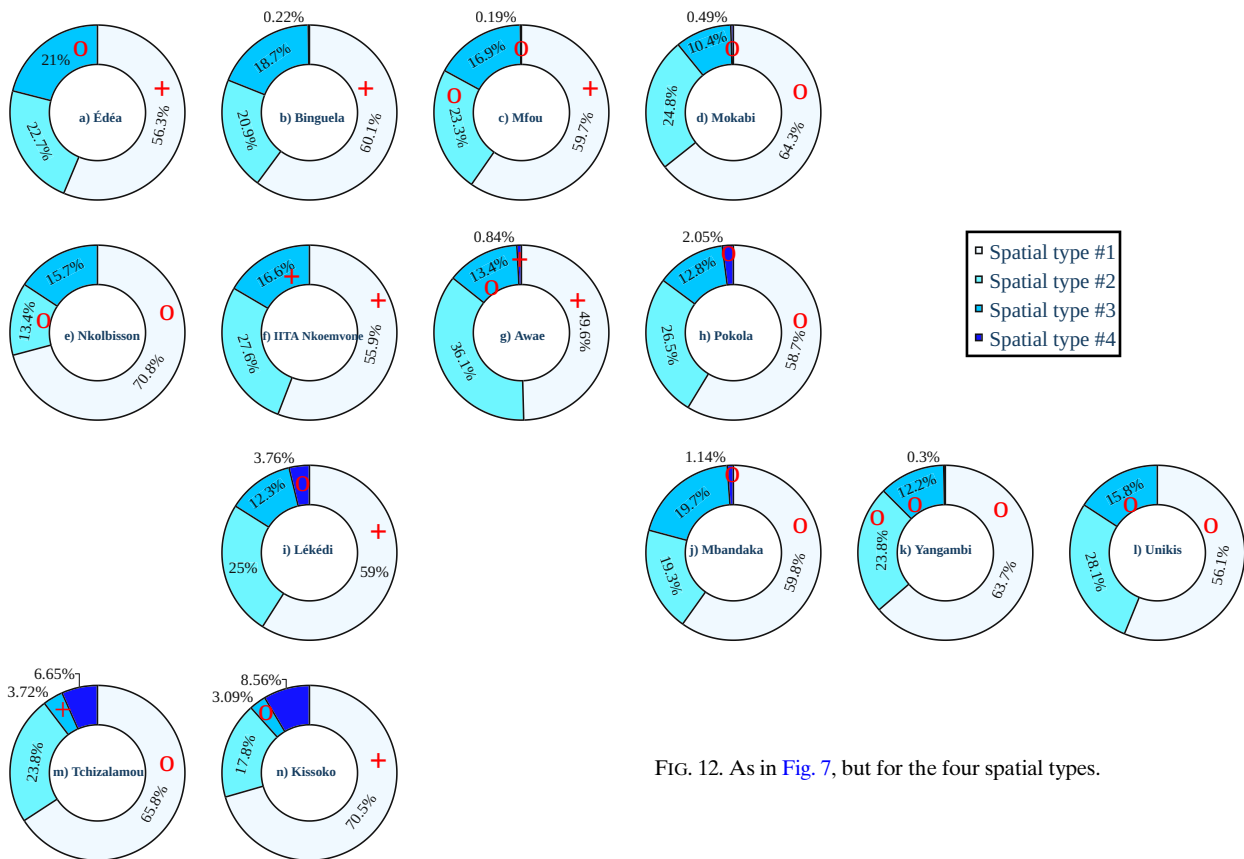
FIG. 12. As in Fig. 7, but for the four spatial types.

	1	2	3	4	5	6
1	2.0 %	-1.0 %	-3.6 %	+ -7.5 %	+ -9.7 %	+ -8.8 %
2	-3.7 %	-1.8 %	+ 3.3 %	+ 26.3 %	+ 11.5 %	+ 24.7 %
3	-3.2 %	+ 8.3 %	+ 13.0 %	+ -10.1 %	+ 16.9 %	+ 1.3 %
4	-2.7 %	+ 4.8 %	+ 5.5 %	+ -7.2 %	+ 66.9 %	+ -7.1 %

FIG. 13. Heatmap of the anomalous probability of co-occurrence of each ST in each spatial type.

This characterization of rainfall events in central Africa provides a basis for future research. The network of rain gauges providing records at high temporal resolution in CA is currently too coarse and documents too short periods, which limits the ability to study the modulation of different types of WEs across the whole region and at the intraseasonal and interannual time scales. Nonetheless, as IMERG continues to provide additional data and the TAHMO station network continues to grow, it should be possible to undertake such intraseasonal and interannual analyses in the near future.

Further work is also needed to understand the atmospheric conditions associated with the different WE types detected, in particular, the dynamic and thermodynamic factors at play.

Data availability statement. The half-hourly rainfall data from Global Precipitation Measurement (GPM) Integrated

Multi-satellitE Retrievals for GPM (IMERG) can be downloaded following https://gpm.nasa.gov/data/directory; the weather stations TAHMO can be accessed through https://tahmo.org/; F-ORE-T weather station data can be obtained on request from http://www.gip-ecofor.org/f-ore-t/reseau.php.

REFERENCES

Adler, R. F., G. Gu, M. Sapiano, J.-J. Wang, and G. J. Huffman, 2017: Global precipitation: Means, variations and trends during the satellite era (1979–2014). *Surv. Geophys.*, **38**, 679–699, https://doi.org/10.1007/s10712-017-9416-4.

Ageet, S., A. H. Fink, M. Maranan, J. E. Diem, J. Hartter, A. L. Ssali, and P. Ayabagabo, 2022: Validation of satellite rainfall estimates over equatorial East Africa. *J. Hydrometeor.*, **23**, 129–151, https://doi.org/10.1175/JHM-D-21-0145.1.

Baidu, M., J. Schwendike, J. H. Marsham, and C. Bain, 2022: Effects of vertical wind shear on intensities of mesoscale convective systems over West and central Africa. *Atmos. Sci. Lett.*, **23**, e1094, https://doi.org/10.1002/asl.1094.

Bigot, S., and Coauthors, 2016: État actuel des réseaux de mesures éco-climatiques en Afrique centrale: Les ambitions du projet de recherche international FORGREENE. *29ème Colloque de l'Association Internationale de Climatologie*. P. Camberlin and Y. Richard (Dijon), Eds., 101–106.

Bulovic, N., N. McIntyre, and F. Johnson, 2020: Evaluation of IMERG V05B 30-min rainfall estimates over the high-elevation tropical Andes mountains. *J. Hydrometeor.*, **21**, 2875–2892, https://doi.org/10.1175/JHM-D-20-0114.1.

Camberlin, P., and Coauthors, 2019: Evaluation of remotely sensed rainfall products over Central Africa. *Quart. J. Roy. Meteor. Soc.*, **145**, 2115–2138, https://doi.org/10.1002/qj.3547.

——, M. Kpanou, and P. Roucou, 2020: Classification of intense rainfall days in southern West Africa and associated atmospheric circulation. *Atmosphere*, **11**, 188, https://doi.org/10.3390/atmos11020188.

——, V. Moron, N. Philippon, F. X. Mengouna, and D. A. Vondou, 2024: Seasonal variations in rain cells propagation over Central Africa and association with diurnal rainfall regimes. *Int. J. Climatol.*, **44**, 2519–2536, https://doi.org/10.1002/joc.8466.

Carvalho, M. J., P. Melo-Gonçalves, J. C. Teixeira, and A. Rocha, 2016: Regionalization of Europe based on a *K*-means cluster analysis of the climate change of temperatures and precipitation. *Phys. Chem. Earth*, **94**, 22–28, https://doi.org/10.1016/j.pce.2016.05.001.

Chen, Y., 2020: Increasingly uneven intra-seasonal distribution of daily and hourly precipitation over Eastern China. *Environ. Res. Lett.*, **15**, 104068, https://doi.org/10.1088/1748-9326/abb1f1.

Cook, K. H., and E. K. Vizy, 2016: The Congo Basin Walker circulation: Dynamics and connections to precipitation. *Climate Dyn.*, **47**, 697–717, https://doi.org/10.1007/s00382-015-2864-y.

Cullmann, J., and Coauthors, 2020: 2020 State of Climate Services: Risk information and early warning systems. WMO/TD-No. 1252, 25 pp., https://library.wmo.int/records/item/57191-2020-state-of-climate-services-risk-information-and-early-warning-systems.

Dezfuli, A. K., 2011: Spatio-temporal variability of seasonal rainfall in western equatorial Africa. *Theor. Appl. Climatol.*, **104**, 57–69, https://doi.org/10.1007/s00704-010-0321-8.

——, C. M. Ichoku, G. J. Huffman, K. I. Mohr, J. S. Selker, N. van de Giesen, R. Hochreutener, and F. O. Annor, 2017: Validation of IMERG precipitation in Africa. *J. Hydrometeor.*, **18**, 2817–2825, https://doi.org/10.1175/JHM-D-17-0139.1.

Farnsworth, A., E. White, C. J. R. Williams, E. Black, and D. R. Kniveton, 2011: Understanding the large scale driving mechanisms of rainfall variability over central Africa. *African Climate and Climate Change*, C. Williams and D. Kniveton, Eds., Advances in Global Change Research, Vol. 43, Springer, 101–122.

Feng, Z., and Coauthors, 2021: A global high-resolution mesoscale convective system database using satellite-derived cloud tops, surface precipitation, and tracking. *J. Geophys. Res. Atmos.*, **126**, e2020JD034202, https://doi.org/10.1029/2020JD034202.

Fotso-Nguemo, T. C., T. Weber, A. Diedhiou, S. Chouto, D. A. Vondou, D. Rechid, and D. Jacob, 2023: Projected impact of increased global warming on heat stress and exposed population over Africa. *Earth's Future*, **11**, e2022EF003268, https://doi.org/10.1029/2022EF003268.

Freitas, E. da S., and Coauthors, 2020: The performance of the IMERG satellite-based product in identifying sub-daily rainfall events and their properties. *J. Hydrol.*, **589**, 125128, https://doi.org/10.1016/j.jhydrol.2020.125128.

Hartman, A. T., 2021: Tracking mesoscale convective systems in central equatorial Africa. *Int. J. Climatol.*, **41**, 469–482, https://doi.org/10.1002/joc.6632.

Hou, A. Y., and Coauthors, 2014: The global precipitation measurement mission. *Bull. Amer. Meteor. Soc.*, **95**, 701–722, https://doi.org/10.1175/BAMS-D-13-00164.1.

Houze, R. A., Jr., 2004: Mesoscale convective systems. *Rev. Geophys.*, **42**, RG4003, https://doi.org/10.1029/2004RG000150.

Hu, H., Z. Feng, and L.-Y. R. Leung, 2021: Linking flood frequency with mesoscale convective systems in the US. *Geophys. Res. Lett.*, **48**, e2021GL092546, https://doi.org/10.1029/2021GL092546.

Huffman, G. J., and Coauthors, 2020: Integrated multi-satellite retrievals for the Global Precipitation Measurement (GPM) mission (IMERG). *Satellite Precipitation Measurement*, V. Levizzani et al. Eds., Advances in Global Change Research, Vol. 67, Springer International Publishing, 343–353.

Igri, P. M., and Coauthors, 2022: Evaluation of the Tropical Rainfall Measuring Mission (TRMM) 3B42 and 3B43 products relative to synoptic weather station observations over Cameroon. *Congo Basin Hydrology, Climate, and Biogeochemistry: A Foundation for the Future*, Geophys. Monogr., Vol. 269, Amer. Geophys. Union, 97–119.

Iroume, J. Y.-A., and Coauthors, 2022: The 21st August 2020 flood in Douala (Cameroon): A major urban flood investigated with 2D HEC-RAS modeling. *Water*, **14**, 1768, https://doi.org/10.3390/w14111768.

Jackson, B., S. E. Nicholson, and D. Klotter, 2009: Mesoscale convective systems over western equatorial Africa and their relationship to large-scale circulation. *Mon. Wea. Rev.*, **137**, 1272–1294, https://doi.org/10.1175/2008MWR2525.1.

Kuete, G., W. Pokam Mba, and R. Washington, 2020: African easterly jet south: Control, maintenance mechanisms and link with Southern subtropical waves. *Climate Dyn.*, **54**, 1539–1552, https://doi.org/10.1007/s00382-019-05072-w.

Laing, A. G., R. E. Carbone, and V. Levizzani, 2011: Cycles and propagation of deep convection over equatorial Africa. *Mon. Wea. Rev.*, **139**, 2832–2853, https://doi.org/10.1175/2011MWR3500.1.

Lengfeld, K., P.-E. Kirstetter, H. J. Fowler, J. Yu, A. Becker, Z. Flamig, and J. Gourley, 2020: Use of radar data for characterizing extreme precipitation at fine scales and short durations. *Environ. Res. Lett.*, **15**, 085003, https://doi.org/10.1088/1748-9326/ab98b4.

Li, R., K. Wang, and D. Qi, 2021: Event-based evaluation of the GPM multisatellite merged precipitation product from 2014 to 2018 over China: Methods and results. *J. Geophys. Res. Atmos.*, **126**, e2020JD033692, https://doi.org/10.1029/2020JD033692.

Livezey, R. E., and W. Y. Chen, 1983: Statistical field significance and its determination by Monte Carlo techniques. *Mon. Wea. Rev.*, **111**, 46–59, https://doi.org/10.1175/1520-0493(1983)111<0046:SFSAID>2.0.CO;2.

Macharia, D., K. Fankhauser, J. S. Selker, J. C. Neff, and E. A. Thomas, 2022: Validation and intercomparison of satellite-based rainfall products over Africa with TAHMO in situ rainfall observations. *J. Hydrometeor.*, **23**, 1131–1154, https://doi.org/10.1175/JHM-D-21-0161.1.

Malhi, Y., S. Adu-Bredu, R. A. Asare, S. L. Lewis, and P. Mayaux, 2013: African rainforests: Past, present and future. *Philos. Trans. Roy. Soc.*, **B368**, 20120312, https://doi.org/10.1098/rstb.2012.0312.

Maranan, M., A. H. Fink, P. Knippertz, L. K. Amekudzi, W. A. Atiah, and M. Stengel, 2020: A process-based validation of GPM IMERG and its sources using a mesoscale rain gauge network in the West African forest zone. *J. Hydrometeor.*, **21**, 729–749, https://doi.org/10.1175/JHM-D-19-0257.1.

Mayaux, P., and Coauthors, 2013: State and evolution of the African rainforests between 1990 and 2010. *Philos. Trans. Roy. Soc.*, **B368**, 20120300, https://doi.org/10.1098/rstb.2012.0300.

Mba, W. P., and Coauthors, 2018: Consequences of 1.5°C and 2°C global warming levels for temperature and precipitation changes over Central Africa. *Environ. Res. Lett.*, **13**, 055011, https://doi.org/10.1088/1748-9326/aab048.

McCollum, J. R., A. Gruber, and M. B. Ba, 2000: Discrepancy between gauges and satellite estimates of rainfall in equatorial Africa. *J. Appl. Meteor.*, **39**, 666–679, https://doi.org/10.1175/1520-0450-39.5.666.

Mengouna, F. X., D. A. Vondou, A. J. K. Mbienda, T. C. Fotso-Nguemo, D. Sonkoué, Z. Yepdo-Djomou, and P. M. Igri, 2022: Influence of "Slab-Ocean" Parameterization in a Regional Climate Model (RegCM4) over Central Africa. *Congo Basin Hydrology, Climate, and Biogeochemistry: A Foundation for the Future, Geophys. Monogr.*, Vol. 269, Amer. Geophys. Union, 49–61.

Monsieurs, E., and Coauthors, 2018: Evaluating TMPA rainfall over the sparsely gauged East African rift. *J. Hydrometeor.*, **19**, 1507–1528, https://doi.org/10.1175/JHM-D-18-0103.1.

Moron, V., R. Barbero, H. J. Fowler, and V. Mishra, 2021: Storm types in India: Linking rainfall duration, spatial extent and intensity. *Philos. Trans. Roy. Soc.*, **A379**, 20200137, https://doi.org/10.1098/rsta.2020.0137.

——, N. Acharya, and S. M. Q. Hassan, 2023: Storm types in Bangladesh: Duration, intensity and area of intra-daily wet events. *Int. J. Climatol.*, **43**, 850–873, https://doi.org/10.1002/joc.7835.

Nesbitt, S. W., R. Cifelli, and S. A. Rutledge, 2006: Storm morphology and rainfall characteristics of TRMM precipitation features. *Mon. Wea. Rev.*, **134**, 2702–2721, https://doi.org/10.1175/MWR3200.1.

Nicholson, S. E., 2022: The rainfall and convective regime over equatorial Africa, with emphasis on the Congo Basin. *Congo Basin Hydrology, Climate, and Biogeochemistry: A Foundation for the Future, Geophys. Monogr.*, Vol. 269, Amer. Geophys. Union, 25–48.

——, D. Klotter, A. K. Dezfuli, and L. Zhou, 2018: New rainfall datasets for the Congo Basin and surrounding regions. *J. Hydrometeor.*, **19**, 1379–1396, https://doi.org/10.1175/JHM-D-18-0015.1.

——, ——, L. Zhou, and W. Hua, 2019: Validation of satellite precipitation estimates over the Congo Basin. *J. Hydrometeor.*, **20**, 631–656, https://doi.org/10.1175/JHM-D-18-0118.1.

O, S., U. Foelsche, G. Kirchengast, J. Fuchsberger, J. Tan, and W. A. Petersen, 2017: Evaluation of GPM IMERG early, late, and final rainfall estimates using WegenerNet gauge data in southeastern Austria. *Hydrol. Earth Syst. Sci.*, **21**, 6559–6572, https://doi.org/10.5194/hess-21-6559-2017.

Orlanski, I., 1975: A rational subdivision of scales for atmospheric processes. *Bull. Amer. Meteor. Soc.*, **56**, 527–530.

Philippon, N., and Coauthors, 2019: The light-deficient climates of western Central African evergreen forests. *Environ. Res. Lett.*, **14**, 034007, https://doi.org/10.1088/1748-9326/aaf5d8.

Pielke, R. A., Jr., and M. W. Downton, 2000: Precipitation and damaging floods: Trends in the United States, 1932–97. *J. Climate*, **13**, 3625–3637, https://doi.org/10.1175/1520-0442(2000)013<3625:PADFTI>2.0.CO;2.

Pokam, W. M., C. L. Bain, R. S. Chadwick, R. Graham, D. J. Sonwa, and F. M. Kamga, 2014: Identification of processes driving low-level westerlies in West Equatorial Africa. *J. Climate*, **27**, 4245–4262, https://doi.org/10.1175/JCLI-D-13-00490.1.

Schneider, U., T. Fuchs, A. Meyer-Christoffer, and B. Rudolf, 2008: Global precipitation analysis products of the GPCC. Global Precipitation Climatology Centre (GPCC), 12 pp.

Schunke, J., P. Laux, J. Bliefernicht, M. Waongo, W. Sawadogo, and H. Kunstmann, 2021: Exploring the potential of the cost-efficient TAHMO observation data for hydro-meteorological applications in Sub-Saharan Africa. *Water*, **13**, 3308, https://doi.org/10.3390/w13223308.

Shige, S., S. Kida, H. Ashiwake, T. Kubota, and K. Aonashi, 2013: Improvement of TMI rain retrievals in mountainous areas. *J. Appl. Meteor. Climatol.*, **52**, 242–254, https://doi.org/10.1175/JAMC-D-12-074.1.

Smith, C., J. C. A. Baker, and D. V. Spracklen, 2023: Tropical deforestation causes large reductions in observed precipitation. *Nature*, **615**, 270–275, https://doi.org/10.1038/s41586-022-05690-1.

Sonwa, D. J., O. A. Somorin, C. Jum, M. Y. Bele, and J. N. Nkem, 2012: Vulnerability, forest-related sectors and climate change adaptation: The case of Cameroon. *For. Policy Econ.*, **23**, 1–9, https://doi.org/10.1016/j.forpol.2012.06.009.

Taguela, T. N., W. M. Pokam, E. Dyer, R. James, and R. Washington, 2022: Low-level circulation over Central Equatorial Africa as simulated from CMIP5 to CMIP6 models. *Climate Dyn.*, **62**, 8333–8351, https://doi.org/10.1007/s00382-022-06411-0.

Tamoffo, A. T., and Coauthors, 2019: Process-oriented assessment of RCA4 regional climate model projections over the Congo Basin under 1.5°C and 2°C global warming levels: Influence of regional moisture fluxes. *Climate Dyn.*, **53**, 1911–1935, https://doi.org/10.1007/s00382-019-04751-y.

Tan, J., W. A. Petersen, and A. Tokay, 2016: A novel approach to identify sources of errors in IMERG for GPM ground validation. *J. Hydrometeor.*, **17**, 2477–2491, https://doi.org/10.1175/JHM-D-16-0079.1.

Tan, M. L., and Z. Duan, 2017: Assessment of GPM and TRMM precipitation products over Singapore. *Remote Sens.*, **9**, 720, https://doi.org/10.3390/rs9070720.

Tang, G., Y. Ma, D. Long, L. Zhong, and Y. Hong, 2016: Evaluation of GPM day-1 IMERG and TMPA version-7 legacy products

over Mainland China at multiple spatiotemporal scales. *J. Hydrol.*, **533**, 152–167, https://doi.org/10.1016/j.jhydrol.2015.12.008.

Tapiador, F. J., R. Roca, A. Del Genio, B. Dewitte, W. Petersen, and F. Zhang, 2019: Is precipitation a good metric for model performance? *Bull. Amer. Meteor. Soc.*, **100**, 223–233, https://doi.org/10.1175/BAMS-D-17-0218.1.

Taylor, C. M., A. H. Fink, C. Klein, D. J. Parker, F. Guichard, P. P. Harris, and K. R. Knapp, 2018: Earlier seasonal onset of intense mesoscale convective systems in the Congo Basin since 1999. *Geophys. Res. Lett.*, **45**, 13 458–13 467, https://doi.org/10.1029/2018GL080516.

Thorndike, R. L., 1953: Who belongs in the family? *Psychometrika*, **18**, 267–276, https://doi.org/10.1007/BF02289263.

Trenberth, K. E., and Y. Zhang, 2018: How often does it really rain? *Bull. Amer. Meteor. Soc.*, **99**, 289–298, https://doi.org/10.1175/BAMS-D-17-0107.1.

Trisos, C. H., and Coauthors, 2022: Africa. *Climate Change 2022: Impacts, Adaptation and Vulnerability*, H.-O. Pörtner et al., Eds., Cambridge University Press, 1285–1455, https://doi.org/10.1017/9781009325844.011.

Upton, G. J. G., 2002: A correlation–regression method for tracking rainstorms using rain-gauge data. *J. Hydrol.*, **261**, 60–73, https://doi.org/10.1016/S0022-1694(01)00618-7.

van de Giesen, N., R. Hut, and J. Selker, 2014: The Trans-African Hydro-Meteorological Observatory (TAHMO). *Wiley Interdiscip. Rev.: Water*, **1**, 341–348, https://doi.org/10.1002/wat2.1034.

Washington, R., and Coauthors, 2006: African climate change: Taking the shorter route. *Bull. Amer. Meteor. Soc.*, **87**, 1355–1366, https://doi.org/10.1175/BAMS-87-10-1355.

——, R. James, H. Pearce, W. M. Pokam, and W. Moufouma-Okia, 2013: Congo Basin rainfall climatology: Can we believe the climate models? *Philos. Trans. Roy. Soc.*, **B368**, 20120296, https://doi.org/10.1098/rstb.2012.0296.

Wilks, D. S., 2011: *Statistical Methods in the Atmospheric Sciences: An Introduction*. Academic Press, 467 pp.

Xing, K., J. R. R. Mayer, and S. Achiche, 2018: Machine tool volumetric error features extraction and classification using principal component analysis and *K*-means. *J. Manuf. Mater. Process.*, **2**, 60, https://doi.org/10.3390/jmmp2030060.

Yepdo Djomou, Z., D. Monkam, and A. Lenouo, 2008: Spatial variability of rainfall regions in West Africa during the 20th century. *Atmos. Sci. Lett.*, **10**, 9–13, https://doi.org/10.1002/asl.202.

You, Y., H. Meng, J. Dong, and S. Rudlosky, 2019: Time-lag correlation between passive microwave measurements and surface precipitation and its impact on precipitation retrieval evaluation. *Geophys. Res. Lett.*, **46**, 8415–8423, https://doi.org/10.1029/2019GL083426.

Zhang, Y., and K. Wang, 2021: Global precipitation system size. *Environ. Res. Lett.*, **16**, 054005, https://doi.org/10.1088/1748-9326/abf394.

Zhou, L., and Coauthors, 2014: Widespread decline of Congo rainforest greenness in the past decade. *Nature*, **509**, 86–90, https://doi.org/10.1038/nature13265.

Zhou, Z., B. Guo, W. Xing, J. Zhou, F. Xu, and Y. Xu, 2020: Comprehensive evaluation of latest GPM era IMERG and GSMaP precipitation products over mainland China. *Atmos. Res.*, **246**, 105132, https://doi.org/10.1016/j.atmosres.2020.105132.